

**SEISMIC TOMOGRAPHY AND ANISOTROPY:
STUDIES OF INTRAPLATE SEISMIC ZONES**

A Dissertation

presented to

the Faculty of the Graduate School

at the University of Missouri-Columbia

In Partial Fulfillment

of the Requirements for the Degree

Doctor of Philosophy

by

QIE ZHANG

Dr. Eric Sandvol, Dissertation Supervisor

DECEMBER 2009

The undersigned, appointed by the dean of the Graduate School, have examined the dissertation entitled

SEISMIC TOMOGRAPHY AND ANISOTROPY: STUDIES OF INTRAPLATE
SEISMIC ZONES

presented by Qie Zhang,

a candidate for the degree of Doctor of Philosophy of Geological Sciences,

and hereby certify that, in their opinion, it is worthy of acceptance.

Professor Eric Sandvol

Professor Mian Liu

Professor Robert Bauer

Professor Francisco Gomez

Professor Zhenbo Qin

ACKNOWLEDGEMENTS

First and foremost, I want to thank my advisor Dr. Eric Sandvol. I did not have any experience in seismology before I started my doctoral research. Dr. Sandvol patiently introduced me into the fascinating world of seismology and guided me through all the difficulties in my research. His scientific ideas and insights were an invaluable resource throughout my five years' study and will be beneficial to my future career.

I would also like to acknowledge the members of my dissertation committee. I want to express my appreciation to Dr. Mian Liu for his constructive and detailed comments on my manuscripts. I want to thank Dr. Robert Bauer, Dr. Francisco Gomez, and Dr. Zhenbo Qin for teaching me the knowledge of geology and math, which has been the basis of my research.

My deepest gratitude goes to my wife, Ya Zhang and my parents for their understanding, dedication, and love. Without their supports, the road towards my doctoral degree would be much bumpier.

TABLE OF CONTENTS

ACKNOWLEDGEMENTS	ii
LIST OF FIGURES	v
ABSTRACT.....	vii
CHAPTER 1: INTRODUCTION.....	1
1.1 INTRAPLATE EARTHQUAKES	1
1.2 SEISMIC TOMOGRAPHY.....	4
1.3 SEISMIC ANISOTROPY	9
1.4 REFERENCES.....	13
CHAPTER 2: TOMOGRAPHIC PN VELOCITY AND ANISOTROPY STRUCTURE IN THE CENTRAL AND EASTERN UNITED STATES	16
2.1 INTRODUCTION	17
2.2 DATA AND METHOD	19
2.3 TOMOGRAPHY AND ANISOTROPY RESULTS	21
2.4 DISCUSSION	25
2.5 CONCLUSIONS	27
2.6 DATA AND RESOURCES	28
2.7 ACKNOWLEDGMENTS	28
2.8 REFERENCES.....	29
CHAPTER 3: LITHOSPHERIC VELOCITY STRUCTURE OF THE NEW MADRID SEISMIC ZONE: A JOINT TELESEISMIC AND LOCAL P TOMOGRAPHIC STUDY	31
3.1 INTRODUCTION	32
3.2 DATA AND MODELS.....	34
3.3 TOMOGRAPHY RESULTS.....	38
3.4 DISCUSSION	43
3.5 CONCLUSIONS	45
3.6 ACKNOWLEDGMENTS	46
3.7 REFERENCES.....	46
CHAPTER 4: RAYLEIGH WAVE TOMOGRAPHY OF THE NORTHEASTERN MARGIN OF THE TIBETAN PLATEAU	50
4.1 INTRODUCTION	51
4.2 DATA COLLECTION AND PROCESSING	56
4.3 METHODOLOGY	58
4.4 RESULTS	62
4.4.1 1-D PHASE VELOCITY MODEL	62
4.4.2 2-D PHASE VELOCITY MODEL	63
4.4.3 1-D SHEAR WAVE VELOCITY MODEL	66
4.4.4 3-D SHEAR WAVE VELOCITY MODEL	68
4.4.5 1-D ANISOTROPY MODEL	70

4.5 DISCUSSION	73
4.6 CONCLUSIONS	79
4.7 ACKNOWLEDGEMENTS	80
4.8 REFERENCES.....	80
CHAPTER 5: CONCLUSIONS	85
5.1 CONCLUSIONS	85
5.2 REFERENCES.....	88
VITA.....	89

LIST OF FIGURES

FIGURE 1.1 REPRODUCTION OF NATIONAL SEISMIC HAZARD MAP OF UNITED STATES FROM PETERSEN ET AL. (2008).....	2
FIGURE 1.2 REPRODUCTION OF SCHEMATIC DIAGRAM OF THE PN RAY PATH FROM LIANG ET AL. (2004).....	6
FIGURE 1.3 REPRODUCTION OF SCHEMATIC DIAGRAM OF THE RAY PATHS OF TELESEISMIC P WAVES AND LOCAL P WAVES FROM THURBER (2003).....	7
FIGURE 1.4 REPRODUCTION OF SCHEMATIC DIAGRAM OF SURFACE WAVE TOMOGRAPHY FOR IMAGING THE ANOMALY FROM NAKANISHI (1993).....	9
FIGURE 2.1 TOPOGRAPHY OF THE CENTRAL AND EASTERN UNITED STATES.....	18
FIGURE 2.2 PN RAY PATHS SELECTED FOR THE ENTIRE MAP	20
FIGURE 2.3 PN VELOCITY VARIATIONS AND CHECKERBORAD TEST	22
FIGURE 2.4 THE NA04 MODEL AT 110 KM AND 150 KM DEPTHS IN THE CEUS	24
FIGURE 2.5 PN ANISOTROPY MODEL FOR THE CEUS	25
FIGURE 3.1 STUDY AREA OF THE NEW MADRID SEISMIC ZONE	33
FIGURE 3.2 LOCATIONS OF 121 TELESEISMIC EVENTS USED TO INVERT FOR THE LITHOSPHERIC VELOCITY STRUCTURES.....	35
FIGURE 3.3 CORRECTION TERMS AT EACH STATION CALCULATED FOR STATION ELEVATION AND SEDIMENT THICKNESS COMBINED USING METHOD M1 AND METHOD M2.....	36
FIGURE 3.4 A 45 KM × 45 KM CHECKERBOARD TEST INVERTED USING THE SAME STATIONS AND EVENTS FOR FIGURES 3.6A AND 3.6B	38
FIGURE 3.5 LEAKING TEST OF THE SEDIMENT.....	39
FIGURE 3.6 LITHOSPHERIC P VELOCITY STRUCTURE FOR THE NMSZ USING SEDIMENT CORRECTION METHODS M1 AND M2	41
FIGURE 3.7 REPRODUCTIONS OF THE PN MODEL AND THE NA04 MODEL IN OUR STUDY AND SURROUNDING AREAS	42
FIGURE 4.1 TOPOGRAPHIC RELIEF OF CHINA AND OUR STUDY AREA.....	56
FIGURE 4.2 LOCATIONS OF 74 TELESEISMIC EVENTS AND GREAT CIRCLE RAY PATHS AT THE PERIODS OF 25, 50, AND 125 S	57
FIGURE 4.3 AVERAGE RAYLEIGH WAVE PHASE VELOCITIES IN OUR STUDY AREA AT 13	

PERIODS RANGING FROM 20 TO 143 s	63
FIGURE 4.4 MAPS OF 2-D ISOTROPIC RAYLEIGH WAVE PHASE VELOCITIES AND THE PHASE VELOCITY UNCERTAINTIES AT 50 s.....	64
FIGURE 4.5 AVERAGE SHEAR WAVE VELOCITIES IN OUR STUDY AREA	67
FIGURE 4.6 MAPS OF 2-D ISOTROPIC SHEAR WAVE VELOCITIES AND MOHO DEPTHS.....	69
FIGURE 4.7 VARIATIONS OF AVERAGE AZIMUTHAL ANISOTROPY WITH PERIODS IN THE WHOLE STUDY AREA, THE NORTHERN STUDY AREA, AND THE SOUTHERN STUDY AREA	72

TOMOGRAPHIC VELOCITY AND ANISOTROPY

STUDIES OF INTRAPLATE SEISMIC ZONES

Qie Zhang

Dr. Eric Sandvol, Dissertation Supervisor

ABSTRACT

Unlike interplate earthquakes which can be readily explained by relative motions at plate boundaries, intraplate earthquakes within stable continents have puzzled scientists for decades. To understand the velocity and anisotropy structures beneath the intraplate seismic zones and further constrain their cause, both body and surface wave tomography has been applied to some of the most significant intraplate seismic zones in the world.

Pn tomography in the Central and Eastern United States reveals that the major intraplate seismic zones at New Madrid, Charleston, East Tennessee, and New England are all near the edges of high-velocity anomalies in the upper mantle. It indicates that the origin of intraplate earthquakes could be related to the rheological boundaries around rigid lithospheric roots where stress may accumulate. This idea is further supported by a Pn anisotropy model that shows large anisotropy (presumably local deformation) surrounding these high-velocity blocks.

A joint teleseismic and local P tomographic study has been performed to explore the enigmatic intraplate earthquakes in the New Madrid seismic zone. The results show that the seismically active zone is associated with a local, NE-SW trending low-velocity

anomaly in the lower crust and upper mantle. Combining the result from Pn tomography, the low-velocity lithosphere is suggestive of a weak zone caused by local deformation due to rheological contrast. This weak source in the lithosphere may shift stress upwards when loaded, thus leading to repeated crustal earthquakes.

The northeastern Tibetan Plateau and North China are other areas where numerous intraplate earthquakes are located. Significant intraplate earthquakes have also occurred at the edges of the Ordos Plateaus and the Sichuan Basin that border the eastern Tibetan Plateau. Rayleigh wave tomography in this area demonstrates the presence of a low-velocity, presumably weak lithosphere beneath the northeastern Tibetan Plateau and a high-velocity, presumably rigid lithosphere beneath the Ordos and Sichuan blocks. Again, the earthquake locations are linked to the low-velocity lithosphere that surrounds rigid lithospheric roots, suggesting that the lithospheric rheology contrast may lead to intraplate seismicity. Moreover, the velocity and anisotropy models imply that an east-southeastward deformation field down to the asthenosphere exists in the study area. This deformation field is possibly associated with the escape tectonics and may also contribute to the occurrence of the intraplate earthquakes.

Chapter 1: INTRODUCTION

1.1 Intraplate Earthquakes

Intraplate earthquakes, in contrast to interplate earthquakes that happen at plate boundaries, are defined to occur in normally stable plate interiors. Unlike frequent interplate earthquakes caused by the significant and persistent relative motions between plates, intraplate earthquakes are rare due to the slow deformation rates at intraplate fault zones. In terms of the numbers, interplate earthquakes at plate margins such as the circum-pacific subduction zone, the San Andreas transform fault, and the mid-ocean ridges, account for more than 90% of all the earthquakes in the world. Intraplate earthquakes that are far away from plate margins, however, only contribute ~0.5% to the global seismic energy release (Johnston and Kanter, 1990). Although intraplate earthquakes are generally sparse and small, sometimes their magnitudes can be very large and cause serious damage to human lives and properties. The New Madrid Seismic Zone (NMSZ) in Missouri and southeastern adjacent states is the largest intraplate seismic zone in the United States. At least three devastating earthquakes ($M \geq 7.0$) occurred here during the winter of 1811-1812 and changed the course of Mississippi river (Johnston, 1996; Petersen et al., 2008). The U.S. Geological Survey reported that the NMSZ is one of the highest hazard zones in its National Seismic Hazard Map (Petersen et al., 2008) (Figure 1.1). Another significant intraplate seismic zone is in Charleston, South Carolina, which was struck by a $M \sim 7.3$ earthquake in 1886 (Johnston, 1996; Petersen et al., 2008). Both the New Madrid and the Charleston regions reach a hazard level comparable to the San Andreas area, the most

intense interplate seismic zone in the United States (Figure 1.1). A few examples of catastrophic intraplate earthquakes in other countries are listed below: the 1920 Haiyuan, China Earthquake (M~7.8) caused a death toll of 200,000; the 1976 Tangshan, China earthquake (M~7.5) took 255,000 people's lives; the 2001 Bhuj, India earthquake (M~7.7) killed >20,000 people; the 2008 Wenchuan, China earthquake (M~7.9) caused 87,587 deaths (http://earthquake.usgs.gov/regional/world/most_destructive.php).

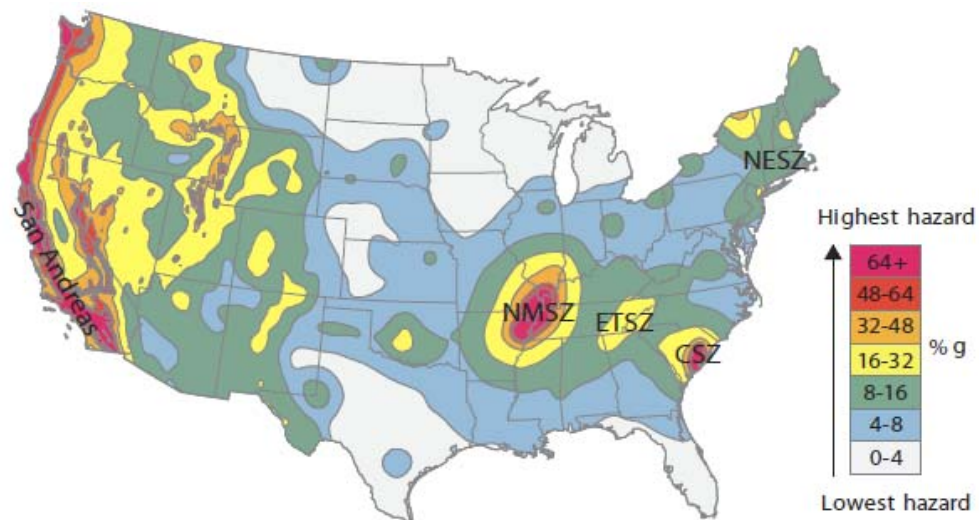


Figure 1.1 Reproduction of National Seismic Hazard Map of United States from Petersen et al. (2008). The intraplate seismic zones are marked as NMSZ (New Madrid Seismic Zone), ETSZ (East Tennessee Seismic Zone), CSZ (Charleston Seismic Zone), and NESZ (New England Seismic Zone). On the western coastline of the map is the interplate seismic zone of the San Andreas transform fault.

To minimize the potential damage, it is important for us to understand the nature and origin of intraplate earthquakes. After decades of research, however, we still know very little about their mechanism. A key disadvantage in solving the problem is the very limited seismic data from intraplate earthquakes due to their much longer recurrence periods compared to interplate earthquakes. For example, the large seismic events in the

NMSZ are expected to only occur for every 500-1000 years (Tuttle et al., 2002; Tuttle et al., 2005; Holbrook et al., 2006; Petersen et al., 2008). Another important factor is that the large recurrence rate allows long-time erosion and sedimentation, which typically bury the surface expression of intraplate earthquake faults. Last, intraplate earthquakes do not seem to necessarily connect with specific geological features, unlike interplate earthquakes that occur along plate boundaries. All of these pose difficulties for the hazard assessment of intraplate earthquakes.

The cause of intraplate earthquakes is under debate. Some scholars attribute it to ancient weak zones such as failed intraplate rifts (Johnston and Kanter, 1990; Johnston et al., 1994). But not all of the ancient rifts are seismogenic, and a recompilation of the global earthquake catalogue within stable continents show that the correlation between the intraplate earthquakes and the ancient rifts may be overestimated (Schulte and Mooney, 2005). Others think intraplate earthquakes may be triggered by a sudden stress change in the lithosphere caused by the post-glacial rebound (Grollimund and Zoback, 2001; Wu and Mazzotti, 2007). Other than those large-scale mechanisms, some local forces have also been considered, including the hypotheses of a recent sinking of the mafic intrusion that provides a gravitational pull (Grana and Richardson, 1996; Pollitz et al., 2001) and a sudden failure of a low-viscosity lower crust which could shift the stress upwards to the upper crust (Kenner and Segall, 2000). All of these hypotheses point to some abnormal structure in the lithosphere such as a weak zone in the lower crust or/and lithospheric mantle.

To identify the seismic velocity anomalies and deformation features that further help constrain the cause of intraplate earthquakes, I have used seismic tomography and

anisotropy measurements to explore the enigmatic intraplate seismic zones. My study has focused on three different areas using three different tomographic methods: (1) Pn tomography and anisotropy in the Central and Eastern United States (Chapter 2) that covers the NMSZ, the Charleston Seismic Zone (CSZ), the East Tennessee Seismic Zone (ETSZ), and the New England Seismic Zone (NESZ), (2) Joint teleseismic and local P tomography in the NMSZ (Chapter 3), and (3) Rayleigh wave (surface wave) tomography and anisotropy in the northeastern Tibetan Plateau (Chapter 4) where intense intraplate seismicity occurred, including the 1920 Haiyuan and 2008 Wenchuan earthquakes. The tomography and anisotropy methods are introduced in the next two sections.

1.2 Seismic Tomography

The word “tomography” was originally used for a medical technique named “computer assisted tomography scan” (CAT-scan) that images human’s internal organs by using X-rays. Seismologists brought the tomography idea into the seismic world in 1974 and published the first series of seismic tomography papers in 1976-1977 (e.g., Aki and Lee, 1976; Aki et al., 1976; Aki et al., 1977). Seismic tomography uses the P and S wave travel times as well as the surface wave data to map the velocity variations of the Earth’s interior. For the studies of earthquake tomography, the receivers are seismometers placed at the surface of the Earth and sources are earthquakes. The observed travel time data or waveform data are then used to invert for the velocity structure sampled by the seismic rays traveling from the earthquakes to the seismometers. The relationship can be expressed mathematically (Menke, 1989):

$$G \bullet \Delta m = \Delta d \quad (1-1)$$

where Δd is the input data vector of residuals (the difference between the observed and predicted travel times or waveforms), Δm is the output model vector of the correction values for the velocity model, and G is the operation matrix of partial derivatives that links Δm to Δd based on the ray paths. The inverse process can be either linear or non-linear determined by the operation matrix G . Seismic tomography theory generally consists of four steps: (1) model parameterization or finding the G matrix, (2) calculating the predicted data vector using current velocity model (forward problem), (3) computing the corrections to the current velocity model using residuals (inverse problem), and (4) testing the model resolution. For most situations, the steps (1) through (3) are run iteratively. The 2-D and 3-D tomographic techniques help us to image the deep velocity structures in the crust and mantle, especially those anomalies associated with temperature change, fluid or partial melting, and subducting slabs. The velocity maps further help us understand the geodynamics between and within the plates as well as the physical processes controlling earthquakes. Different scales of the tomographic models are constructed by utilizing various seismic waves and different epicentral distances. The three tomographic methods used in my studies are briefly described below with schematic figures. More details can be found in the chapters 2-4.

Pn tomography utilizes the Pn phase (body wave) from regional seismograms to measure the 2-D lateral velocity variations in the uppermost mantle. Pn phase is a head wave that dives towards the Moho, then bends and travels horizontally along the top of the mantle, and finally bends up towards the receiver (Hearn, 1996; Liang et al., 2004) (Figure 1.2). The horizontal segment right beneath the Moho is used for mapping the

velocity perturbations in the lithospheric mantle. The earthquakes with epicentral distances between 2° and 14° are typically used to make sure that the Pn phase is the first arrival, which avoids the contamination from other phases. An advantage of Pn tomography is that it uses absolute travel times, so absolute velocities are resolved. I have applied Pn tomography to the Central and Eastern United States to construct a 2-D large-scale velocity map of the upper mantle (Chapter 2).

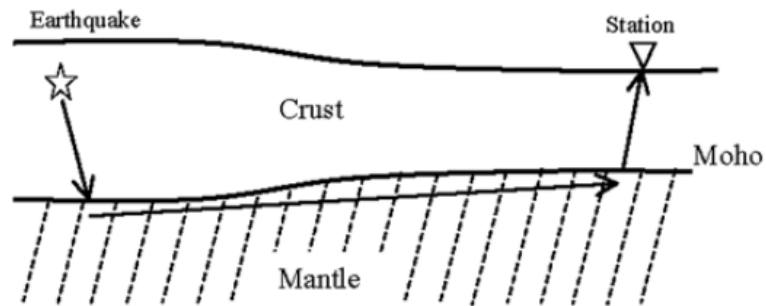


Figure 1.2 Reproduction of schematic diagram of the Pn ray path from Liang et al. (2004).

Teleseismic tomography is also called ACH tomography, named after the first formal tomographic paper (Aki et al., 1977). It uses teleseismic events that are often restricted with greater than 25° epicentral distances (Figure 1.3a). The large distances of the earthquakes allow us to assume that the seismic rays approach the stations as plane-waves and the relative travel time residuals are only a result of the velocity structure immediately beneath the local network of stations (Figure 1.3a). Thus, only relative travel times are considered for the inversion, and the precise locations and origin times of the sources are not important. The first arrival P wave is the most frequently used phase for teleseismic tomography. Based on the similarity of the teleseismic

waveforms, the relative travel times can be measured very precisely through a cross-correlation technique (VanDecar, and Crosson, 1990) that provides far more accurate readings than absolute travel time measurements. The maximum depth that teleseismic tomography can image varies from around one hundred kilometers to more than one thousand kilometers, depending on the size of the array. Because the incident rays are almost vertical, the vertical resolution of teleseismic tomography is generally poor.

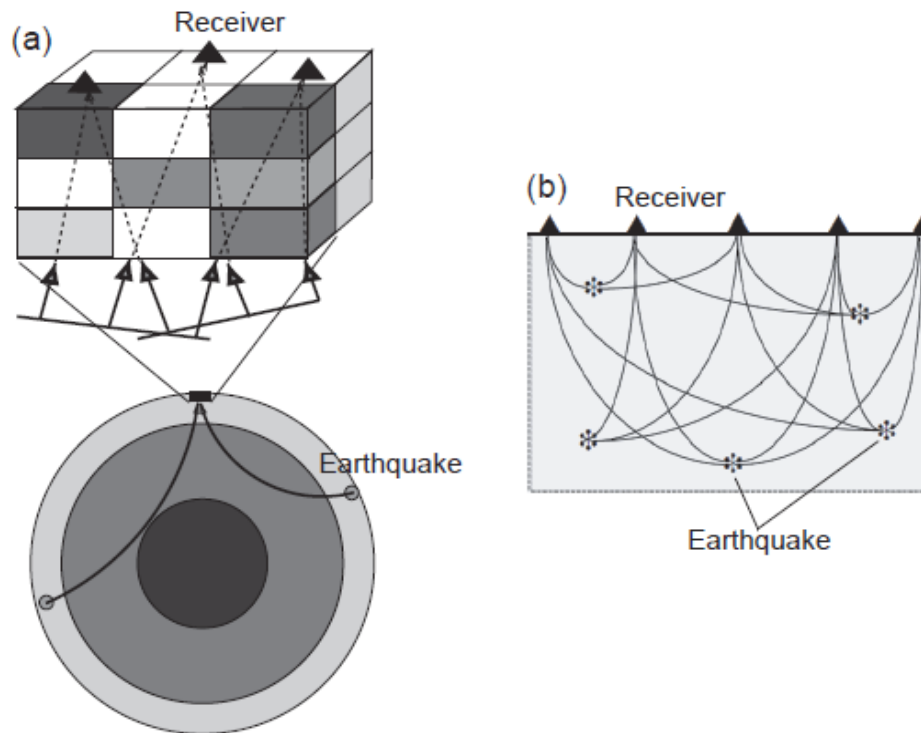


Figure 1.3 Reproduction of schematic diagram of the ray paths of teleseismic P waves (a) and local P waves (b) from Thurber (2003).

Local tomography uses the absolute travel times (P or S waves) from local events to measure the velocity structures beneath the array (Figure 1.3b). Both events and

receivers are within the study velocity model. Because each entire ray path from the source to the receiver accounts for the travel time residual, the location and the origin time of every earthquake needs to be precisely known. The largest depth of the local tomographic model is limited to the maximum event depth that varies from tens of kilometers to hundreds of kilometers. Because the seismic rays cross one another quite often, the local tomography has better vertical resolution. Sometimes it is important to include the local data in the teleseismic tomography because the local data help constrain the shallow velocity structure. The joint teleseismic and local P wave tomography has been applied to the New Madrid Seismic Zone to image its lithospheric structure down to 160 km (Chapter 3).

Surface wave tomography utilizes Rayleigh waves or Love waves that propagate basically along the great circle paths of the Earth to map the phase or group velocities beneath the great circles (Figure 1.4). Because surface waves at a particular period are most sensitive to the velocity structure at the depth of their $\sim 1/3$ wavelength, the phase or group velocity variations with periods allow us to calculate the velocity model as a function of depth. As a standard process, the dispersion curve (the phase or group velocities at a series of periods) at each map point is taken to determine the shear wave velocities by a 1-D inversion. All the map points are later gathered to construct a 3-D shear wave velocity model in the study area. Traditional surface wave tomography uses either a single-station method or a two-station method. The single-station method needs an accurate knowledge of the source information, and the two-station method requires both stations to be at the same great circle from the source. These limitations greatly restrict the application of the surface wave tomography. A recent two-plane wave

approach (Yang and Forsyth, 2006) helps to take the advantage of the recorded information at all stations and exclude the influence of scattering and multipathing outside of the array. This advanced approach has been applied to my Rayleigh wave tomography study in the northeastern Tibetan Plateau (Chapter 4).

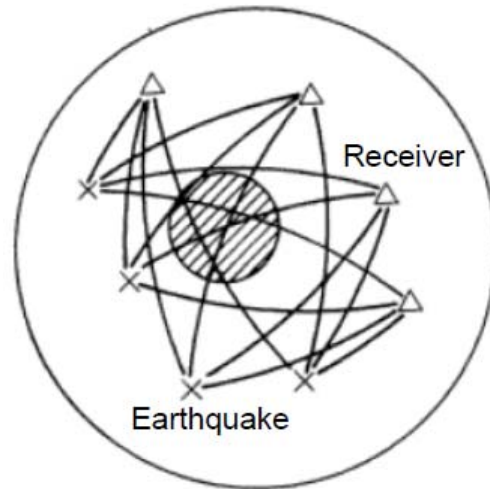


Figure 1.4 Reproduction of schematic diagram of surface wave tomography for imaging the anomaly (shaded circle) from Nakanishi (1993). Note that the rays propagate along great circles at the Earth's surface.

1.3 Seismic Anisotropy

Seismic anisotropy, defined as the dependence of seismic wavespeed on the direction of propagation, is a very important tool for imaging the deformation of the Earth's interior. Although the origin of the anisotropy is not yet clearly resolved, the major cause is typically considered to be either shape-preferred orientation (SPO) or lattice-preferred orientation (LPO) (Fouch and Rondenay, 2006). The SPO is related to the cracks or inclusions such as fluid-filled cracks in the continental crust and melt-filled cracks in the

mid-ocean ridges. In the situation, the seismic fast direction is generally parallel to the crack plane, i.e., the compressional stress orientation. Normally, the SPO is thought to be only a local and shallow feature beneath continents (Fouch and Rondenay, 2006). In the upper mantle, where the high pressure forces the cracks to close, the LPO (alignment of anisotropic minerals) becomes the primary source for the seismic anisotropy. Studies have shown that the upper mantle (from Moho to ~660 km) accounts for most of the anisotropy beneath continents, while the crustal contribution is typically very small (Silver, 1996; Fouch et al., 2000). The highly anisotropic and dominant mineral in the upper mantle, olivine, is believed to be the main candidate for the LPO-caused anisotropy. The crystallographic axes of olivine are usually orientated according to the surrounding strain, so the seismic anisotropy caused by the olivine LPO can help us infer the internal deformation in the upper mantle. Two different hypotheses have been suggested for explaining the LPO-caused anisotropy beneath continents. The first hypothesis considers the anisotropy to be a “fossil” fabric in the lithosphere that records recent large tectonic events such as mountain building (Silver, 1996; Savage, 1999; Fouch et al., 2000). It is an appropriate explanation when the anisotropy matches the surficial geological observations, for example, when the fast seismic direction is parallel to the orogen strike, i.e., the extensional stress orientation. The other hypothesis suggests that the fast seismic direction presents the sub-lithospheric or asthenospheric flow direction (Silver, 1996; Savage, 1999; Fouch et al., 2000). It explains the situation when the fast direction is consistent with the Absolute Plate Motion (APM).

Four common methods for imaging the continental seismic anisotropy (Park and Levin, 2002; Fouch and Rondenay, 2006) have been summarized here. (1) Shear wave

splitting, the most popular and unambiguous method, measures the fast shear wave direction and the travel lag time between the fast and slow split shear waves by using SKS phase primarily (e.g., Silver and Chan, 1991). Although powerful for resolving anisotropy, the splitting parameters only present the integrated anisotropy characteristic along the ray path, and thus do not provide the depth location of the anisotropy. (2) Resolving anisotropy terms simultaneously with the velocity terms during the tomographic inversion. This method has been applied to both Pn and Rayleigh wave tomography for resolving azimuthal anisotropy (e.g., Hearn, 1996; Yang and Forsyth, 2006). The anisotropy from Pn tomography provides a 2-D map of the lateral anisotropy variations right beneath the Moho, so it directly measures the anisotropy of the upper mantle. On the other hand, the Rayleigh wave tomographic inversion is able to resolve the azimuthal anisotropy at various periods. Therefore, it provides the depth constraints for anisotropy. The main limitation of the anisotropy measurements from both Pn and Rayleigh wave tomography is the trade-off between the anisotropy and velocity terms. (3) Anisotropy can also be measured through the observation of the variations of relative P or S wave delay times as a function of the azimuth and incidence angle of the incoming rays (e.g., Babuska and Cara, 1991). When teleseismic data in an appropriate distance range are used, the dipping axes of the anisotropy can be resolved. This method is less used compared to the previous two methods. Again, the major drawback of this method is still the trade-off between the anisotropy and the unknown velocity anomalies. (4) Recent receiver function technique takes the advantage of the Ps converted waveform (P wave to S wave) at the abrupt discontinuity to evaluate the anisotropy media (e.g., Savage, 1998). The negative attribute is that this method is an under-determined inverse problem.

For my studies, I have used method (2) with the tomography access to infer the anisotropy models. The anisotropy parameterizations in the Pn tomography and Rayleigh wave tomography have a close format. For the Pn tomography, the slowness (inverse of velocity) in each inversion cell is expressed as:

$$S = S_0 + A \cos(2\theta) + B \sin(2\theta) \quad (1-2)$$

where S_0 is the azimuthally averaged Pn slowness (i.e., isotropic component), A and B are the azimuthal anisotropic coefficients, θ is the back azimuth angle, and the high-order terms are neglected (e.g., Hearn, 1996). During the inversion, the slowness parameter S_0 and the anisotropy parameters A and B are resolved simultaneously. The fast seismic direction is defined by the θ value that minimizes the slowness S (or maximizes the velocity). So, take the derivative of equation (1-2) and set it to zero:

$$\frac{dS}{d\theta} = -2A \sin(2\theta) + 2B \cos(2\theta) = 0 \quad (1-3)$$

Then, we have:

$$2\theta = \tan^{-1}\left(\frac{B}{A}\right) + k\pi \quad (1-4)$$

where k is any integer. Therefore, the solution is given by one of the two orthogonal azimuths:

$$\theta = \frac{1}{2} \tan^{-1}\left(\frac{B}{A}\right) \text{ or } \frac{1}{2} \tan^{-1}\left(\frac{B}{A}\right) + \frac{\pi}{2} \quad (1-5)$$

The fast seismic direction is the θ value in equation (1-5) that yields the smallest slowness S in equation (1-2). The peak-to-peak anisotropy magnitude (the difference between the fastest velocity and the slowest velocity) is then given by:

$$M = 2\sqrt{A^2 + B^2} \quad (1-6)$$

For the Rayleigh wave tomography, the velocity at each node is parameterized in the same way as in equation (1-2) (e.g., Yang and Forsyth, 2006):

$$C(\omega, \theta) = C_0(\omega) + A(\omega)\cos(2\theta) + B(\omega)\sin(2\theta) \quad (1-7)$$

where the phase velocity C instead of the slowness S is used, and the C value depends on the frequency ω . The solution of the fast direction for each frequency is still calculated by equation (1-5), but the θ value maximizing the phase velocity C is chosen. The formula of anisotropy magnitude follows equation (1-6). The advantage of the anisotropy information resolved at different frequencies in Rayleigh wave tomography allows us to constrain the anisotropy depths.

1.4 References

- Aki, K., and W.H.K. Lee (1976), Determination of three-dimensional anomalies under a seismic array using first P arrival times from local earthquakes, 1. A homogeneous initial model, *J. Geophys. Res.*, 81, 4381-4399.
- Aki, K., A. Christoffersson, and E. Husebye (1976), Three-dimensional seismic structure under the Montana LASA, *Bull. Seism. Soc. Am.*, 66, 501-524.
- Aki, K., A. Christoffersson, and E.S. Husebye (1977), Determination of the three-dimensional seismic structure of the lithosphere, *J. Geophys. Res.*, 82, 277-296.
- Babuska, V., and M. Cara, (1991), Seismic anisotropy in the earth. *Modern Approaches in Geophysics*, vol. 10, Kluwer, Boston.
- Fouch, M.J., K.M. Fischer, E.M. Parmentier, M.E. Wysession, and T.J. Clarke (2000), Shear wave splitting, continental keels, and patterns of mantle flow, *J. Geophys. Res.*, 105, 6255-6275.
- Fouch, M.J., and S. Rondenay (2006), Seismic anisotropy beneath stable continental interiors, *Phys. Earth Planet. In.*, 158, 292-320.
- Grana, J.P., and R.M. Richardson (1996), Tectonic stress within the New Madrid seismic zone, *J. Geophys. Res.*, 101, 5445-5458.

- Grollimund, B., and M.D. Zoback (2001), Did deglaciation trigger intraplate seismicity in the New Madrid seismic zone? *Geology*, 29, 175-178.
- Hearn, T.M. (1996), Anisotropic Pn tomography in the western United States, *J. Geophys. Res.*, 101, 8403-8414.
- Holbrook, J., W.J. Autin, T.M. Rittenour, S. Marshak, and R.J. Goble (2006), Stratigraphic evidence for millennial-scale temporal clustering of earthquakes on a continental-interior fault: Holocene Mississippi River floodplain deposits, New Madrid seismic zone, USA, *Tectonophysics*, 420, 431-454.
- Johnston, A.C., and L.R. Kanter (1990), Earthquakes in stable continental crust, *Sci. Am.*, 262, 68-75.
- Johnston, A.C., K.J. Coppersmith, L.R. Kanter, and C.A. Cornell (1994), The earthquakes of stable continental regions: assessment of large earthquake potential, TR-102261, Vol. 1-5, Ed. J. F. Schneider, *Elect. Power Res. Inst. (EPRI)*, Palo Alto, CA, 309p.
- Johnston, A.C. (1996), Seismic moment assessment of earthquakes in stable continental regions-III. New Madrid 1811-1812, Charleston 1886 and Lisbon 1755, *Geophys. J. Int.*, 126, 314-344.
- Kenner, S.J., and P. Segall (2000), A mechanical model for intraplate earthquakes: Application to the New Madrid Seismic Zone, *Science*, 289, 2329-2332.
- Liang, C., X. Song, and J. Huang (2004), Tomographic inversion of Pn travel times in China, *J. Geophys. Res.*, 109, B11304, doi:10.1029/2003JB002789.
- Menke, W. (1989), *Geophysical data analysis: discrete inverse theory*, revised edition, *Academic Press Inc.*, New York, 285p.
- Nakanishi, I. (1993), Surface wave tomography: velocity and Q, in *Seismic tomography: theory and practice*, Chapman and Hall, London, United Kingdom, 92-132.
- Park, J., and V. Levin (2002), Seismic anisotropy: tracing plate dynamics in the mantle, *Science*, 296, 485-489.
- Petersen, M.D., A.D. Frankel, S.C. Harmsen, C.S. Mueller, K.M. Haller, R.L. Wheeler, R.L. Wesson, Y. Zeng, O.S. Boyd, D.M. Perkins, N. Luco, E.H. Field, C.J. Wills, and K.S. Rukstales (2008), Documentation for the 2008 Update of the United States National Seismic Hazard Maps, *U.S. Geological Survey Open-File Report 2008-1128*, 61p.
- Pollitz, F.F., L. Kellogg, and R. Burgmann (2001), Sinking mafic body in a reactivated lower crust: A mechanism for stress concentration at the New Madrid Seismic Zone, *Bull. Seismol. Soc. Am.*, 91, 1882-1897.

- Savage, M.K. (1998), Lower crustal anisotropy or dipping boundaries? Effects on receiver functions and a case study in New Zealand, *J. Geophys. Res.*, 103, 15,069-15,087.
- Savage, M.K. (1999), Seismic anisotropy and mantle deformation: What have we learned from shear wave splitting? *Rev. Geophys.*, 37, 65-106.
- Schulte, S.M., and W.D. Mooney (2005), An updated global earthquake catalogue for stable continental regions: reassessing the correlation with ancient rifts, *Geophys. J. Int.*, 161, 707-721.
- Silver, P.G., and W.W. Chan (1991), Shear wave splitting and subcontinental mantle deformation, *J. Geophys. Res.*, 96, 16,429-16,454.
- Silver, P.G. (1996), Seismic anisotropy beneath the continents: Probing the depths of geology, *Annu. Rev. Earth Planet. Sci.*, 24, 385-432.
- Thurber, C.H. (2003), Seismic tomography of the lithosphere with body waves, *Pure Appl. Geophys.*, 160, 717-737.
- Tuttle, M.P., E.S. Schweig, J.D. Sims, R.H. Lafferty, L.W. Wolf, and M.L. Haynes (2002), The earthquake potential of the New Madrid Seismic Zone, *Bull. Seismol. Soc. Am.*, 92, 2080-2089.
- Tuttle, M.P., E.S. Schweig III, J. Campbell, P.M. Thomas, J.D. Sims, and R.H. Lafferty III (2005), Evidence for New Madrid earthquakes in A.D. 300 and 2350 B.C., *Seismol. Res. Lett.*, 76, 489-501.
- VanDecar, J.C., and R.S. Crosson (1990), Determination of teleseismic relative phase arrival times using multi-channel cross-correlation and least squares, *Bull. Seismol. Soc. Am.*, 80, 150-169.
- Wu, P., and S. Mazzotti (2007), Effects of a lithospheric weak zone on postglacial seismotectonics in eastern Canada and the northeastern United States, in *Continental Intraplate Earthquakes: Science, Hazard, and Policy Issues, Spec. Pap. Geol. Soc. Am.*, 425, 113-128.
- Yang, Y., and D.W. Forsyth (2006), Rayleigh wave phase velocities, small-scale convection, and azimuthal anisotropy beneath southern California, *J. Geophys. Res.*, 111, B07306, doi:10.1029/2005JB004180.

CHAPTER 2: TOMOGRAPHIC P_n VELOCITY AND ANISOTROPY STRUCTURE IN THE CENTRAL AND EASTERN UNITED STATES

Qie Zhang, Eric Sandvol, and Mian Liu

Reproduced by permission of Seismological Society of America (*Bulletin of the Seismological Society of America*, 2009)

Abstract. A total of 19,166 P_n phase readings from the International Seismological Centre (ISC) and the National Earthquake Information Center (NEIC) catalogs as well as hand-picked arrivals from the Incorporated Research Institutions for Seismology (IRIS) Data Management Center were inverted to map the velocity and anisotropy structure of the lithospheric mantle in the central and eastern United States (CEUS). Our P_n tomographic model shows a broad region of very fast velocity under the North American craton (the northern CEUS) and significant lateral variations within the rest of the CEUS. The surface locations of the major intraplate seismic zones are near the edges of high-velocity anomalies, which is consistent with the notion that stress accumulation and hence focused deformation are likely to occur at the rheological boundaries around the rigid lithospheric root. However, the ancient rifts show no clear correlation to the low-velocity anomalies in the lithospheric mantle. Our P_n anisotropic model shows a complex pattern of fast directions with an overall north–south trend in the CEUS that may reflect the preserved

fabrics of the cratonic lithosphere. Nonetheless, high Pn anisotropy seems to wrap around the high-velocity blocks, which may indicate local deformation around the rigid blocks.

2.1 Introduction

The central and eastern United States (CEUS), defined as east of the Rocky Mountains, is considered tectonically stable in contrast to the active western United States (Figure 2.1). The northern part of the CEUS is dominated by the North American craton, with a cold, rigid lithosphere up to 250 km thick (Grand, 1994; Van der Lee and Nolet, 1997). To the east and west, the craton is bordered by the orogenic belts of the Appalachians and the Rocky Mountains, respectively. Although Cenozoic crustal deformation is minimal, there are several major seismogenic zones in the CEUS (Figure 2.1): the New Madrid seismic zone (NMSZ), the east Tennessee seismic zone (ETSZ), the Charleston seismic zone (CSZ), and the New England seismic zone (NESZ). The mechanics of these intraplate earthquakes remain poorly understood. It is recognized that some seismic zones are associated with failed rifts or ancient plate boundaries within the CEUS (Figure 2.1). For example, the NMSZ is within the northern Reelfoot rift (RR), and the ETSZ is close to the East Continent rift (ECR). These ancient rifts may represent weak zones and hence are prone to earthquakes (Johnston and Kanter, 1990). In particular, previous studies of seismic velocity structure and heat flow have suggested that the RR is warm and weak (Al-Shukri and Mitchell, 1987; Liu and Zoback, 1997).

However, not all of the ancient rifts are seismogenic, and their correlation may be overestimated (Schulte and Mooney, 2005). In particular, McKenna et al. (2007) have

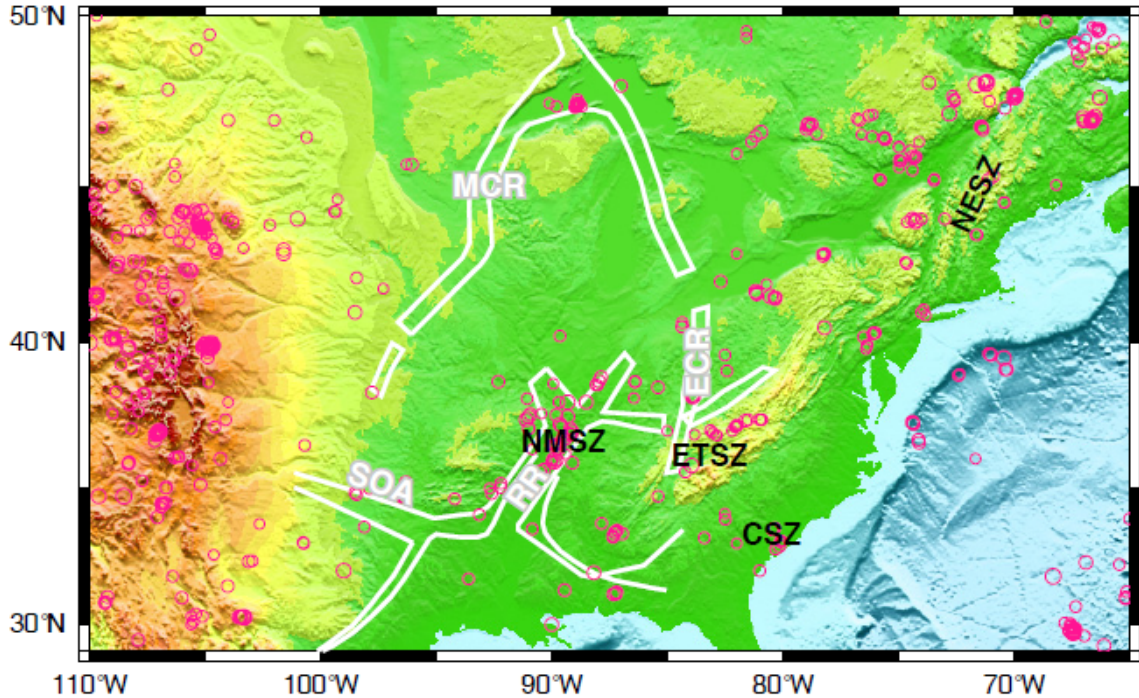


Figure 2.1 Topography of the central and eastern United States (CEUS). The white lines are the approximate boundaries of the ancient rift zones: RR denotes the Reelfoot rift, MCR the Mid-Continent rift, ECR the East Continent rift, and SOA the Southern Oklahoma Aulacogen. The circles are the earthquake locations from the ISC catalog (1964–2000) with magnitudes of at least 4. The major intraplate seismic zones in the study area are NMSZ (New Madrid seismic zone), ETSZ (East Tennessee seismic zone), CSZ (Charleston seismic zone), and NESZ (New England seismic zone).

argued against warm and weak rift zones in the NMSZ. The correlations between the seismic zones in the CEUS and the lithospheric structure have not been well established at the regional scale. Previous research on the large-scale lithospheric tomography of the CEUS mainly focused on the shear-wave velocity models by studying Sn, S, and Rayleigh waves (e.g., Grand, 1994; Alsina et al., 1996; Van der Lee and Nolet, 1997; Nolet et al., 1998; Van der Lee and Frederiksen, 2005). The global P-wave tomographic research for this region primarily consists of teleseismic P velocity models (e.g., Bijwaard et al., 1998; Vasco and Johnson, 1998; Zhao, 2004). These studies show significant lateral velocity

variations of the lithospheric structure in the CEUS, but their correlations to the seismic zones remain unclear.

The Pn wave travels horizontally within the lithospheric mantle and is therefore an excellent source for mapping the lateral velocity variations of the lithosphere. By jointly inverting for Pn velocity and anisotropy, we will refine the structure of the lithospheric mantle in the CEUS. More importantly, we will explore the potential relationship among the Pn velocity anomalies, the ancient rifts, and the major seismic zones, attempting to understand the nature of the intraplate earthquakes and the lithospheric deformation in the CEUS.

2.2 Data and Method

Our study area of the CEUS (29°–50° N, 65°–110° W) is shown in Figure 2.2. To avoid smearing edge effects in tomography, we collected data from a much broader area (20°–60° N, 55°–115° W). From the catalogs of the International Seismological Centre (ISC) and the National Earthquake Information Center (NEIC) (see the Data and Resources section), 27,190 Pn ray paths were collected following these strict criteria: (1) first arrivals with epicentral distances from 2° to 14°, (2) events shallower than 35 km, (3) events located within a 0.1° precision, (4) events recorded within a 0.1 sec precision, (5) picks within a 0.1 sec precision, (6) a minimum of six event records for each station and six station records for each event, and (7) ISC assigned residuals within 10 sec. In addition, we manually picked 776 Pn arrivals of the waveform dataset from the Incorporated Research Institutions for Seismology (IRIS) (see the Data and Resources section) to supplement the

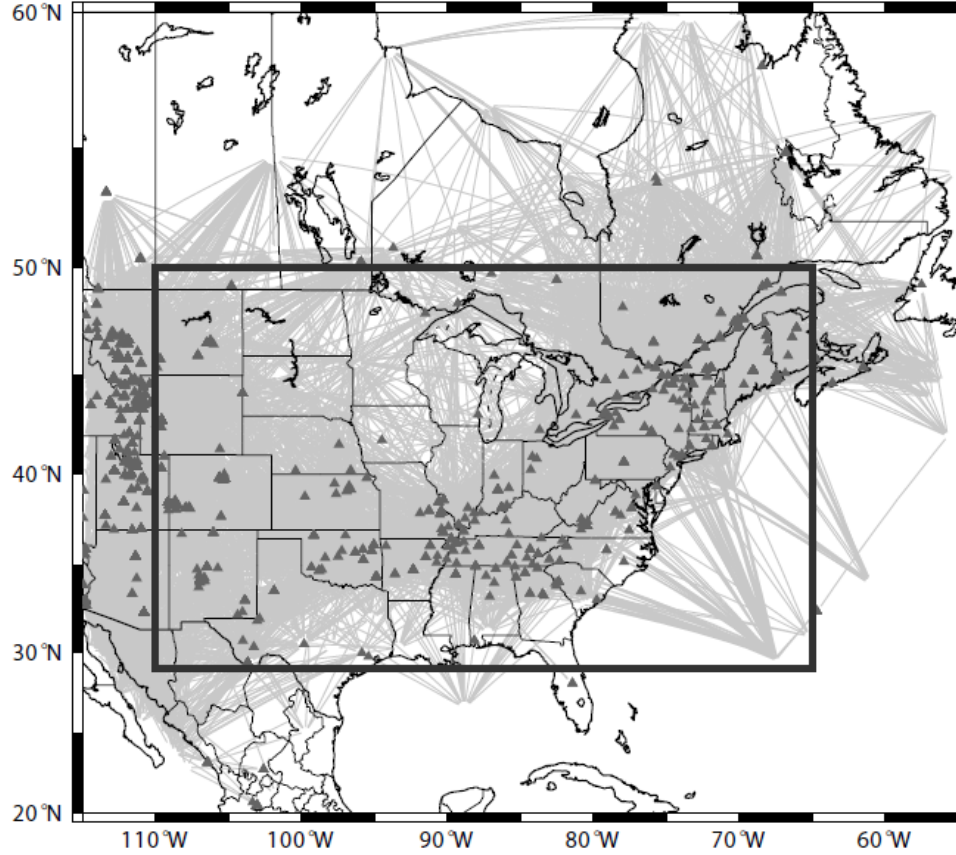


Figure 2.2 Pn ray paths selected for the entire map (20°–60° N, 55°–115° W) containing 19,166 individual event-station pairs. The inner rectangle box shows our study area (29°–50° N, 65°–110° W). Solid triangles are the seismic stations used in this study.

ISC and the NEIC dataset as well as to test their quality. Finally, by applying a 6 sec residual cut to the straight line fit of the travel times versus distance, 19,166 Pn-phase readings were screened out for the inversion of our models. This fit line yielded an average Pn velocity of 8.1 km/sec in the study area.

We followed the Pn tomography and anisotropy technique developed by Hearn (1996). The Pn travel-time residual (t_{ij}) is described by the travel-time equation:

$$t_{ij} = a_i + b_j + \sum d_{ijk} (s_k + A_k \cos 2\phi + B_k \sin 2\phi)$$

where a_i and b_j are the static delays for station i and event j , respectively, d_{ijk} is the

distance traveled by ray ij in mantle cell k , s_k is the slowness in cell k , A_k and B_k are the anisotropy coefficients, and ϕ is the back azimuth angle. A $0.5^\circ \times 0.5^\circ$ cell size was chosen for our study area. Slowness and anisotropy values in each cell were iteratively resolved by using the LSQR algorithm (Paige and Saunders, 1982a,b). During the inversion, Laplacian damping was used to control the smoothness of both the velocity and anisotropy models. After the inversion, our tomographic model achieved a 35.7% variance reduction from the starting model.

Figure 2.2 shows the ray paths of all event-station pairs. Note that, except along southern coastlines of the United States and the region west of the Great Lakes, the majority of our study area is covered by a high density of ray paths, which ensures a model of robust resolution.

2.3 Tomography and Anisotropy Results

The Pn tomographic image and the checkerboard test are shown in Figure 2.3. The checkerboard model (Figure 2.3b) was synthesized by alternating high and low velocities in $3.3^\circ \times 3.3^\circ$ cells and then inverting with the same ray paths to test the reliability of our tomographic inversion. A conservative level of Gaussian noise (1.5 sec) was added during the synthetic test, which was chosen to be larger than the root mean squares of the residuals after the true inversion (1.3 sec). Even with such a high level of noise, the alternating patterns were well recovered for most areas.

Figure 2.3a shows Pn velocity variations with respect to 8.1 km/sec. The results generally agree with the shear-wave velocity structure of the NA04 model at 110 and 150

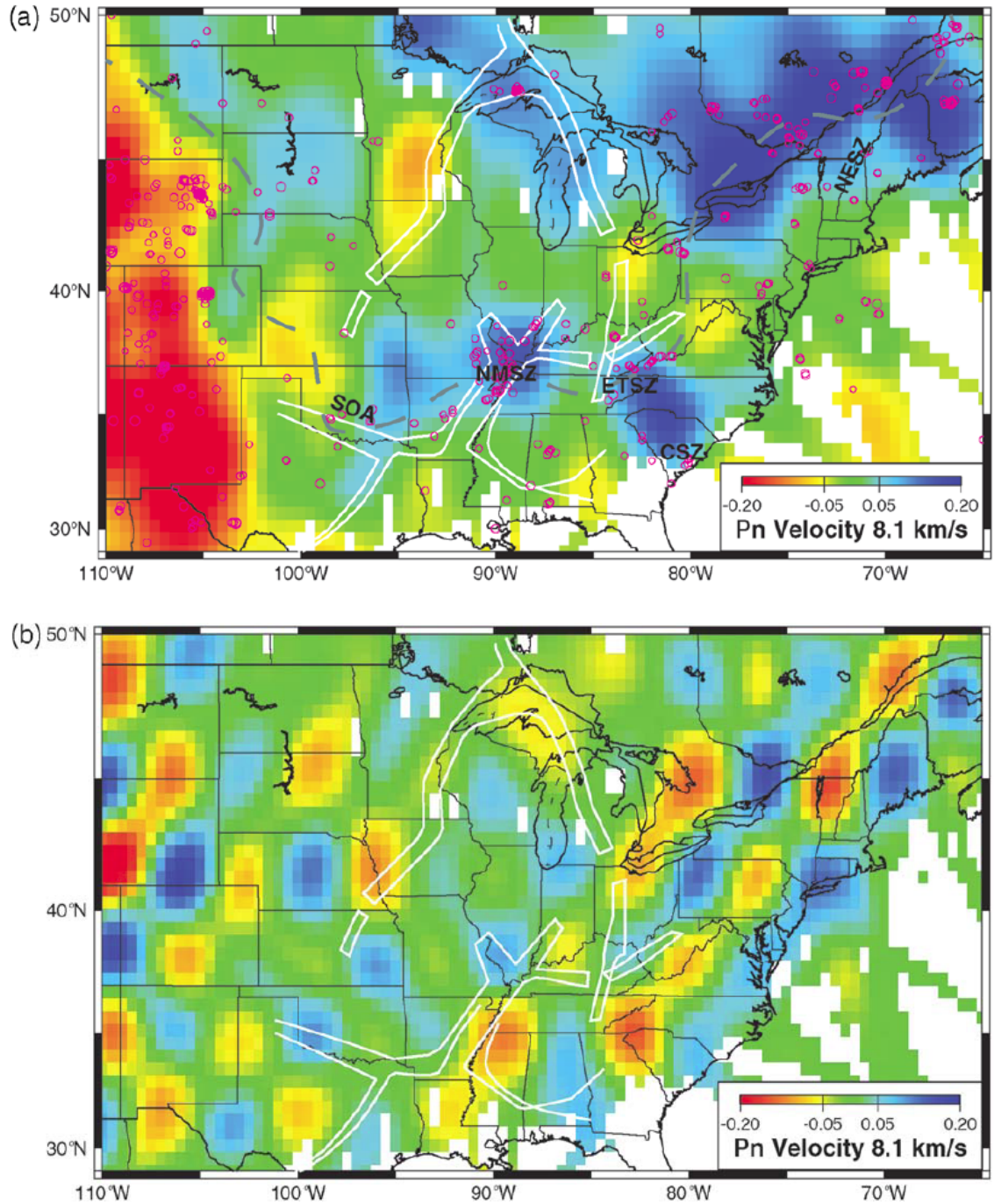


Figure 2.3 (a) Pn velocity variations obtained from the inversion of travel-time data for the CEUS. The dashed gray line delimits the +0.1 km/sec contour of the high-velocity lithosphere in the NA04 model at 110 km depth for comparison. Note that main intraplate seismic zones (NMSZ, ETSZ, CSZ, and NESZ) are near the margins of the high-velocity anomalies. (b) A $3.3^\circ \times 3.3^\circ$ checkerboard test inverted using the same stations and events for Figure 2.3a. Gaussian noise with a standard deviation of 1.5 sec was added during the synthetic test.

km depths (Van der Lee and Frederiksen, 2005; see the Data and Resources section) (Figure 2.4), but with more detailed variations. Both ours and the NA04 model show a very high velocity (8.2–8.3 km/sec) under the Precambrian North American craton in the northern CEUS. At the western boundary of the craton, both models display a sharp velocity change between the low-velocity Rocky Mountains and the high-velocity craton. On the eastern edge of the craton, our Pn model shows two moderately low-velocity blocks (8.0–8.1 km/sec) in southern New England and southern Pennsylvania, respectively. These relatively low-velocity anomalies have also been indicated in other tomographic studies (e.g., Levin et al., 1995; Li et al., 2003; Van der Lee and Frederiksen, 2005). The edges of these two low anomalies seem to delineate the eastern boundary of the craton.

Along the northwestern boundary of the Mississippi embayment, our Pn tomography shows an east–west-oriented high-velocity belt (8.2–8.3 km/sec), extending from the NMSZ to the Southern Oklahoma Aulacogen (SOA) seismic zone (Figure 2.3a). This belt also appears in the NA04 model. Our Pn image shows a high-velocity anomaly (8.2–8.3 km/sec) in North and South Carolina, opposite to the NA04 model. Within the craton, our Pn model shows low velocities beneath the left leg of the Mid-Continent rift (MCR) and northern Ohio. Similar trends are shown in the NA04 model with somewhat shifted local velocity minima.

Figure 2.5 shows our Pn anisotropic model that was obtained by simultaneously inverting for both velocity and anisotropy. The pattern of the fast directions is complex with an overall north–south trend. Some local areas with strong Pn anisotropy are also found to be associated with the margins of the high-velocity blocks, where intraplate seismicity occurs nearby.

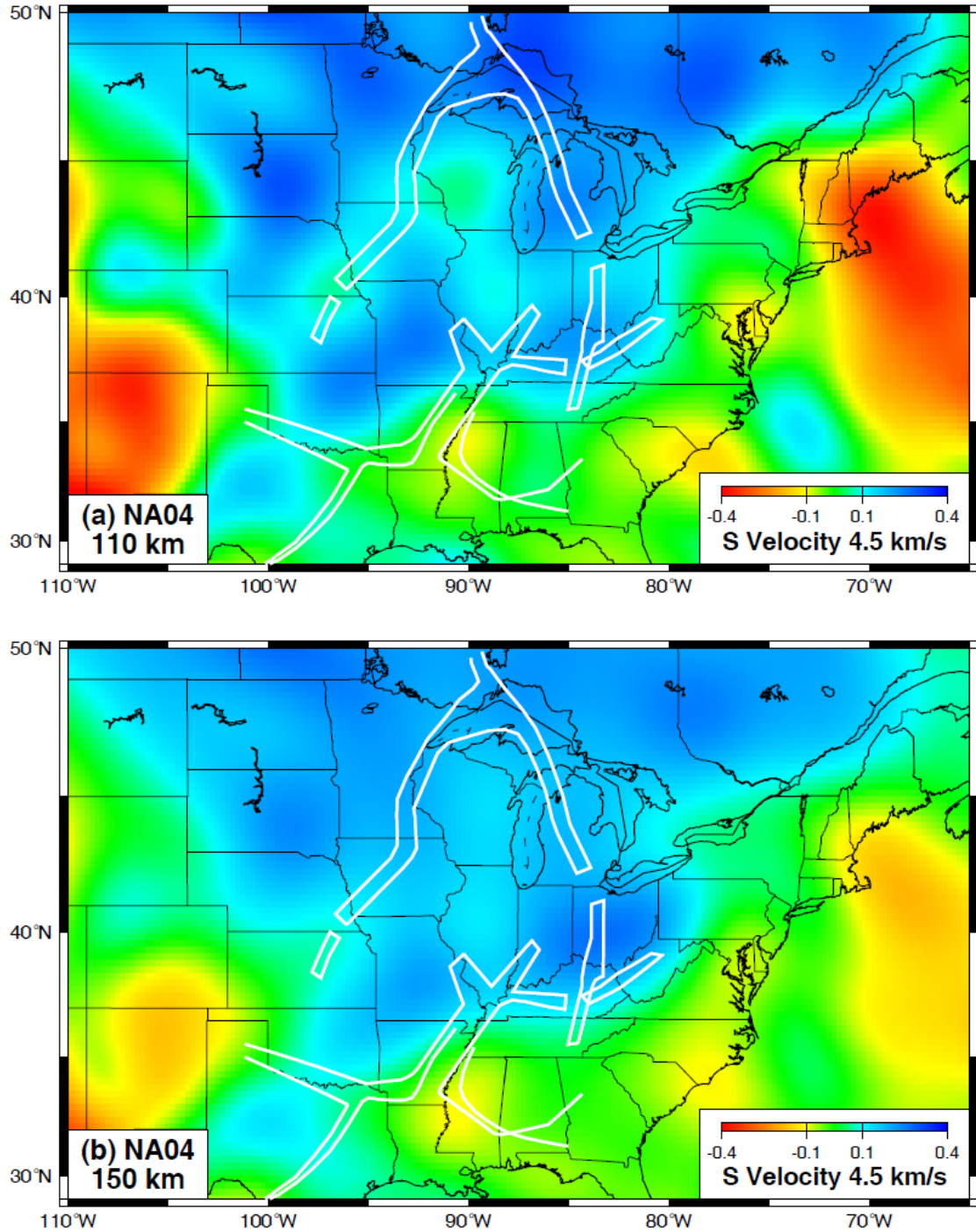


Figure 2.4 (a) The NA04 model at 110 km depth in the CEUS. The white lines are the approximate boundaries of the ancient rift zones. The NA04 model shows a broad high velocity underneath the craton in the northern CEUS. The +0.1 km/s contour relative to the reference velocity (4.5 km/s) is plotted in our Pn velocity image (Figure 2.3a of the text) for the comparison of the high velocity lithosphere boundary. For more detailed comparison results, refer to the text. (b) The NA04 model at 150 km depth in the CEUS. The velocity variation patterns are similar to those at 110 km depth.

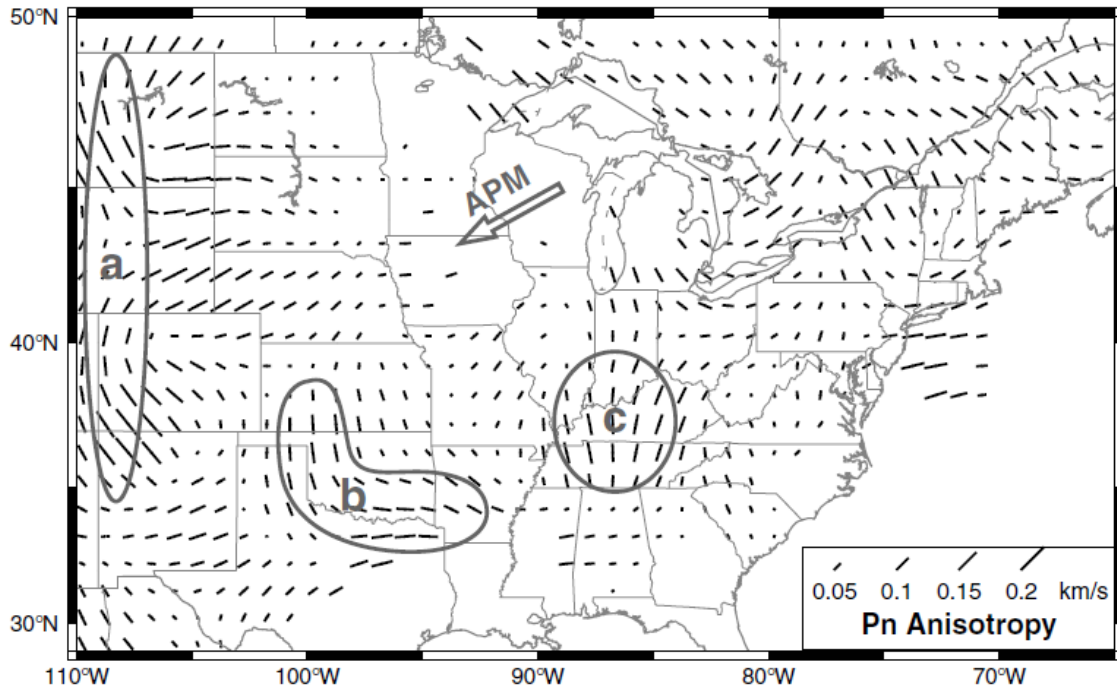


Figure 2.5 Pn anisotropy model for the CEUS. This model was created by simultaneously inverting for Pn anisotropy and velocity. Only cells with more than 10 counts were plotted. The strikes of the vectors show the fast directions, and their lengths are proportional to the amount of anisotropy. The large arrow gives the absolute plate motion (APM) of North America. Circled areas a, b, and c are where strong anisotropy occurs, which may indicate focused deformation.

2.4 Discussion

Our Pn tomography model has mapped a clear velocity contrast of lithospheric mantle along 105° W: low velocity under the Rocky Mountains on the west and high velocity under the stable craton on the east (Figure 2.3a). Within the rigid CEUS, major seismic zones are found near the margins of very high-velocity anomalies: the NESZ is within the edge of the North American craton; the NMSZ is right on a very high-velocity block, while the significant earthquakes occurred at the southwestern edge of the block; the ETSZ, the CSZ, and the SOA all align along the boundaries of fast anomalies. In general,

most of the large seismic events are located at the edge or just within the high-velocity anomalies in the CEUS. Interestingly, similar correlations have been found in some significant intraplate seismic zones elsewhere. For example, large earthquakes concentrated on the edge of the rigid Ordos Plateau in northern China (Pei et al., 2007), and intense seismicity in the Kutch region, western India, also occurred on the margin of a high-velocity anomaly of lithospheric mantle (Kennett and Widiyantoro, 1999). This observation is consistent with the notion that stress tends to concentrate in the rheological boundaries (Lowry and Smith, 1995). When the lateral rheological variation of the lithospheric root is not considered, Li et al.'s (2007) numerical model predicts high deviatoric stresses around the margins of the thick cratonic lithosphere in the CEUS.

On the other hand, the intracontinental rifts show no consistent correlation with low-velocity anomalies (Figure 2.3a), contrary to common perceptions (Johnston and Kanter, 1990; Liu and Zoback, 1997). The eastern leg of the MCR is underlain by a high-velocity anomaly, whereas its western leg is underlain by a low-velocity anomaly. The northern and southern ECR are underlain by low and normal velocities, respectively. The RR is associated with very high lithospheric velocity, contrary to some previous results (Al-Shukri and Mitchell, 1987; Liu and Zoback, 1997).

Our Pn anisotropy image (Figure 2.5) indicates stronger anisotropy in the Rocky Mountains (area a) than in the craton, and the fast direction generally follows the boundary at 105° W. This result is consistent with the idea that hotter and possibly weaker lithospheric mantle deforms more coherently than the lithospheric root underlying the cratonic regions. Within the CEUS, our anisotropy model shows a complex pattern with a generally north–south direction at a high angle to the direction of absolute plate motion

(APM). It is consistent with the result of Marone and Romanowicz (2007), who proposed that in the upper 200 km of the North American craton, the azimuthal anisotropy reflects a preserved fabric characteristic of the cratonic lithosphere.

The local variations of our anisotropy seem to correlate with the Pn velocity anomalies. The strong anisotropy in areas b and c (Figure 2.5) occurs in the regions of locally relatively low velocities, and its fast direction wraps around the high-velocity blocks. Note that area b is on the edge of the NMSZ and the SOA; area c is between the NMSZ and the ETSZ. These patterns may indicate focused deformation around the rigid blocks, which could contribute to stress concentration and hence large earthquakes in the crust.

2.5 Conclusions

Using Pn travel-time data, we have constructed a Pn tomographic model that shows the lateral lithospheric velocity structure in the CEUS. The model does not support the perception that the ancient rifts in the CEUS correlate with low-velocity anomalies, or weak zones in the lithospheric mantle. Based on the lack of spatial association between the ancient rifts and the major intraplate seismic zones in the CEUS, we suggest that the ancient rifts are not the primary factor causing the large seismic events in the CEUS.

However, we found a strong correlation between the lateral velocity variations and the significant intraplate seismicity: the major seismic zones tend to occur near the edges of the high-velocity anomalies in the lithospheric mantle. This correlation may be explained by the stress concentration near rheological boundaries and the tendency of more rigid

lithosphere to host large earthquakes.

Our Pn anisotropy results also indicate focused mantle flow around the edges of the high-velocity blocks. Such mantle shearing may have further contribution to the stress localization and intraplate seismicity in the CEUS.

2.6 Data and Resources

Travel-time readings used in this study were collected from the ISC catalog available at www.isc.ac.uk and the NEIC catalog available at www.earthquake.usgs.gov/regional/neic. Waveform data were obtained from the IRIS Data Management Center at www.iris.edu. The NA04 velocity anomaly data came from Suzan van der Lee's personal website, www.earth.northwestern.edu/current/people/faculty/suzan/na04.tar.gz. All of the figures were made using the Generic Mapping Tools (GMT) (www.soest.hawaii.edu/gmt; Wessel and Smith, 1998).

2.7 Acknowledgments

We would like to thank Associate Editor Diane Doser and reviewer Catherine Snelson for their very helpful comments. This work was partially supported by U.S. Geological Survey National Earthquake Hazards Reduction Program Grant Number 04HQGR0046.

2.8 References

- Al-Shukri, H.J., and B.J. Mitchell (1987), Three-dimensional velocity variations and their relation to the structure and tectonic evolution of the New Madrid seismic zone, *J. Geophys. Res.*, 92, 6377–6390.
- Alsina, D., R.L. Woodward, and R.K. Snieder (1996), Shear wave velocity structure in North America from large-scale waveform inversions of surface waves, *J. Geophys. Res.*, 101, no. B7, 15,969–15,986.
- Bijwaard, H., W. Spakman, and E.R. Engdahl (1998), Closing the gap between regional and global travel time tomography, *J. Geophys. Res.*, 103, no. B12, 30,055–30,078.
- Grand, S.P. (1994), Mantle shear structure beneath the Americas and surrounding oceans, *J. Geophys. Res.*, 99, no. B6, 11,591–11,621.
- Hearn, T.M. (1996), Anisotropic Pn tomography in the western United States, *J. Geophys. Res.*, 101, no. B4, 8403–8414.
- Johnston, A.C., and L. R. Kanter (1990), Earthquakes in stable continental crust, *Sci. Am.*, 262, 68–75.
- Kennett, B.L.N., and S. Widiyantoro (1999), A low seismic wavespeed anomaly beneath northwestern India: a seismic signature of the Deccan plume?, *Earth Planet. Sci. Lett.*, 165, 145–155.
- Levin, V., A. Lerner-Lam, and W. Menke (1995), Anomalous mantle structure at the Proterozoic–Paleozoic boundary in northeastern US, *Geophys. Res. Lett.*, 22, 121–124.
- Li, A., D.W. Forsyth, and K.M. Fischer (2003), Shear velocity structure and azimuthal anisotropy beneath eastern North America from Rayleigh wave inversion, *J. Geophys. Res.*, 108, no. B8, 2362, doi 10.1029/2002JB002259.
- Li, Q., M. Liu, Q. Zhang, and E. Sandvol (2007), Stress evolution and seismicity in the central-eastern United States: insights from geodynamic modeling, in Continental Intraplate Earthquakes: Science, Hazard, and Policy Issues, *Geol. Soc. Am. Special Paper*, 425, 149–166.
- Liu, L., and M. Zoback (1997), Lithospheric strength and intraplate seismicity in the New Madrid seismic zone, *Tectonics*, 16, 585–595.
- Lowry, A.R., and R.B. Smith (1995), Strength and rheology of the western U.S. Cordillera, *J. Geophys. Res.*, 100, no. B9, 17,947–17,963.

- Marone, F., and B. Romanowicz (2007), The depth distribution of azimuthal anisotropy in the continental upper mantle, *Nature*, 447, 198–201.
- McKenna, J., S. Stein, and C.A. Stein (2007), Is the New Madrid seismic zone hotter and weaker than its surroundings?, in *Continental Intraplate Earthquakes: Science, Hazard, and Policy Issues*, *Geol. Soc. Am. Special Paper*, 425, 167–175.
- Nolet, G., C. Coutlee, and R. Clouser (1998), Sn velocities in western and eastern North America, *Geophys. Res. Lett.*, 25, 1557–1560.
- Paige, C.C., and M.A. Saunders (1982a), LSQR: an algorithm for sparse linear equations and least squares problems, *ACM Trans. Math. Softw.*, 8, no. 1, 43–71.
- Paige, C.C., and M.A. Saunders (1982b), LSQR: sparse linear equations and least squares problems, *ACM Trans. Math. Softw.*, 8, no. 2, 195–209.
- Pei, S., J. Zhao, Y. Sun, Z. Xu, S. Wang, H. Liu, C.A. Rowe, M.N. Toksöz, and X. Gao (2007), Upper mantle seismic velocities and anisotropy in China determined through Pn and Sn tomography, *J. Geophys. Res.*, 112, B05312, doi 10.1029/2006JB004409.
- Schulte, S.M., and W.D. Mooney (2005), An updated global earthquake catalogue for stable continental regions: reassessing the correlation with ancient rifts, *Geophys. J. Int.*, 161, 707–721.
- Van der Lee, S., and A. Frederiksen (2005), Surface wave tomography applied to the North American upper mantle, in *Seismic Data Analysis and Imaging with Global and Local Arrays*, G. Nolet and A. Levander (Editors), *American Geophysical Monograph*, 157, 67–80.
- Van der Lee, S., and G. Nolet (1997), Upper mantle S velocity structure of North America, *J. Geophys. Res.*, 102, no. 22, 815–22,838.
- Vasco, D.W., and L.R. Johnson (1998), Whole Earth structure estimated from seismic arrival times, *J. Geophys. Res.*, 103, 2633–2671.
- Wessel, P., and W.H.F. Smith (1998), New, improved version of Generic Mapping Tools released, *Eos Trans. AGU*, 79, no. 47, 579.
- Zhao, D. (2004), Global tomographic images of mantle plumes and subducting slabs: insight into deep Earth dynamics, *Phys. Earth Planet. Int.*, 146, 3–34.

CHAPTER 3: LITHOSPHERIC VELOCITY STRUCTURE OF THE NEW MADRID SEISMIC ZONE: A JOINT TELESEISMIC AND LOCAL P TOMOGRAPHIC STUDY

Qie Zhang, Eric Sandvol, and Mian Liu

Reproduced by permission of American Geophysical Union (*Geophysical Research Letters*, 2009)

Abstract. The enigmatic seismicity in the New Madrid Seismic Zone (NMSZ) has been attributed to some abnormal lithospheric structure, including the presence of dense mafic intrusions and a low-viscosity lower crust. However, the area's detailed lithospheric structure remains unclear. Here we invert 2,056 teleseismic P and 12,226 local P first arrival times from a recent nine-year dataset to infer the lithospheric velocity structure beneath the NMSZ. Our results show that the seismically active zone is associated with a local, NE–SW trending low-velocity anomaly in the lower crust and upper mantle, instead of high-velocity intrusive bodies proposed in previous studies. The low-velocity anomaly is on the edge of a high-velocity lithospheric block, consistent with the notion of stress concentration near rheological boundaries. This lithospheric weak zone may shift stress to the upper crust when loaded, thus leading to repeated shallow earthquakes.

3.1 Introduction

The New Madrid Seismic Zone (NMSZ), located in the northern Mississippi embayment, is the most seismically active region in the Central and Eastern United States (CEUS) (Figure 3.1). A sequence of at least three major earthquakes ($M_w \geq 7.0$) occurred here during the winter of 1811–1812 (Johnston and Schweig, 1996), and thousands of microearthquakes have been recorded since 1974. The microseismicity delineates three linear faults in the NMSZ (Figure 3.1): (1) the NE-trending Blytheville Fault Zone (BFZ), (2) the NW-trending Reelfoot Fault (RF), and (3) the NNE-trending New Madrid North Fault (NN) (Johnston and Schweig, 1996). The largest events including the 1811–1812 main shocks (Johnston and Schweig, 1996; Hough et al., 2003), the 1843 Marked Tree, Arkansas earthquake ($M \sim 6.3$), and the 1895 Charleston, Missouri earthquake ($M \sim 6.6$) (Johnston, 1996) are thought to have occurred on those faults (Figure 3.1). Paleoseismologic studies also suggest that several large earthquakes similar to the 1811–1812 sequence have happened in the NMSZ in the past a few thousand years (Tuttle et al., 2002).

The cause of these intraplate earthquakes remains uncertain. The NMSZ is located within the Reelfoot rift (Ervin and McGinnis, 1975) which may be related to the seismicity (Johnston and Kanter, 1990), but not all rifts in the CEUS are seismic (Li et al., 2007). The surface deformation associated with the NMSZ is minimal, and recent GPS studies, while differing in details, show near zero site velocities outside the NMSZ (Newman et al., 1999; Smalley et al., 2005; Calais et al., 2005; Calais and Stein, 2009). Hence some “deep” and “local” causes have been suggested to explain the seismicity. One such cause is a recent change to the dense Proterozoic-Cambrian mafic intrusions that provides a localized

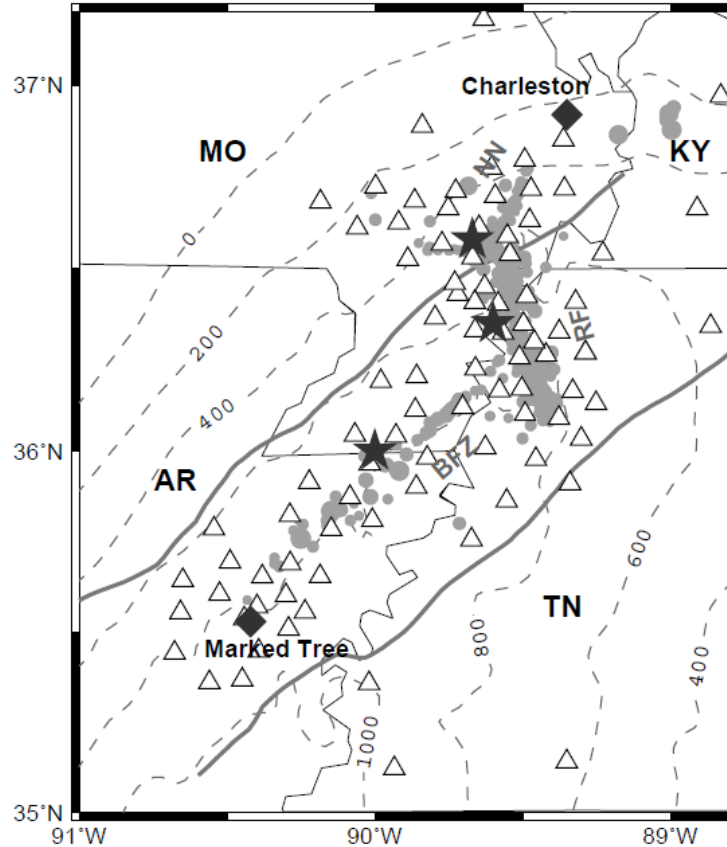


Figure 3.1 Study area (35° – 37.2° N, 88.8° – 91° W) of the New Madrid Seismic Zone (NMSZ). The triangles are the seismic stations for both teleseismic and local records. The solid dots are the local events ($M \leq 3.9$) recorded during 1999–2007 used for our tomographic inversion. Those microearthquakes delineate three linear segments: the BFZ (Blytheville Fault Zone), the RF (Reelfoot Fault), and the NN (New Madrid North Fault) (Johnston and Schweig, 1996). Three stars show the estimated epicenters of the 1811–1812 $M_w \geq 7.0$ events (Johnston and Schweig, 1996; Hough et al., 2003). Two diamonds show the estimated locations of the 1843 Marked Tree, Arkansas earthquake ($M \sim 6.3$) and the 1895 Charleston, Missouri earthquake ($M \sim 6.6$), respectively (Johnston, 1996). Two thick grey lines delineate the boundaries of the Reelfoot rift. The dashed lines delineate sediment thickness contours (200 m interval) extracted from Bodin et al.’s (2001) contour data.

gravitational force in the rift (Grana and Richardson, 1996; Pollitz et al., 2001); another is low-viscosity lower crust (and probably low-viscosity upper mantle too) under the NMSZ that can shift deviatoric stresses imposed by tectonic (stress or thermal) perturbations to the upper crust to trigger a sequence of earthquakes (Kenner and Segall, 2000). However, the

details of lithospheric structure under the NMSZ are not clear. Mitchell and co-workers found some low-velocity anomalies in the NMSZ lithosphere (Mitchell et al., 1977; Al-Shukri and Mitchell, 1987), but the resolution of their models is limited due to the data available at that time.

In this study we use a new dataset recorded between 1999 and 2007 from the Cooperative New Madrid Seismic Network (Figure 3.1) operated by the Center for Earthquake Research and Information (CERI) to map the lithospheric structure beneath the NMSZ. The network contains three times the number of seismic stations in a much more focused study area compared to Al-Shukri and Mitchell's (1987).

3.2 Data and Models

From this new dataset, we extracted both teleseismic and local P first arrivals for the joint tomographic inversion. We picked 121 teleseismic events (Figure 3.2) using the criteria of (1) magnitude $M_b \geq 5.0$, (2) epicenter distance $\geq 25^\circ$, and (3) recording station number ≥ 8 . Theoretical first arrival-times of teleseismic P phases were calculated from the AK135 model (Kennett et al., 1995), and then relative travel-time residuals were measured for each event by a semi-automated method, Multi-Channel Cross-Correlation (MCCC) (VanDecar and Crosson, 1990). We modified the method by running the MCCC multiple times with shift corrections for all correlation windows after each run. When the shift corrections converge to zero, the correlation windows used for calculating relative delays are adjusted to the right corresponding positions. This procedure improves the measurements by up to 0.5 sec. During the process, we used a threshold value (0.06 sec) of

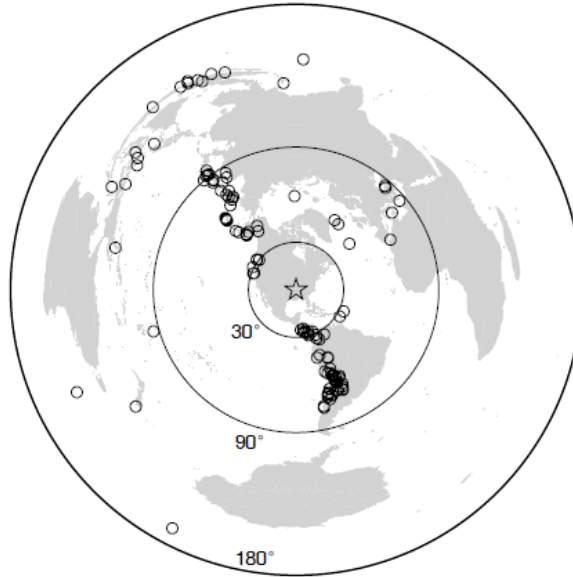


Figure 3.2 Locations of 121 teleseismic events (the circles) used to invert for the lithospheric velocity structures. The star stands for the study area of the NMSZ.

root-mean-square timing uncertainty (VanDecar and Crosson, 1990) to rule out the low-quality waveforms. A total of 2,056 accurate teleseismic P travel-times were selected for this study. 95% of the teleseismic residuals relative to the network mean vary within a range of ± 0.5 sec.

The poor vertical resolution of teleseismic tomography can be improved by including local P phases to constrain the shallow velocity structure and separate the residual contributions between the crust and mantle. We extracted local P picks from the CERI catalog with the following requirements: (1) pick accuracy within 0.35 sec, (2) a minimum of 8 recording stations for each event, and (3) a minimum of 8 event records for each station. Those criteria yielded 12,226 first P arrivals associated with 684 local events (Figure 3.1), whose maximum depth is at 26 km. In total, we obtained 14,282 joint first arrival measurements of teleseismic and local P phases for our inversion.

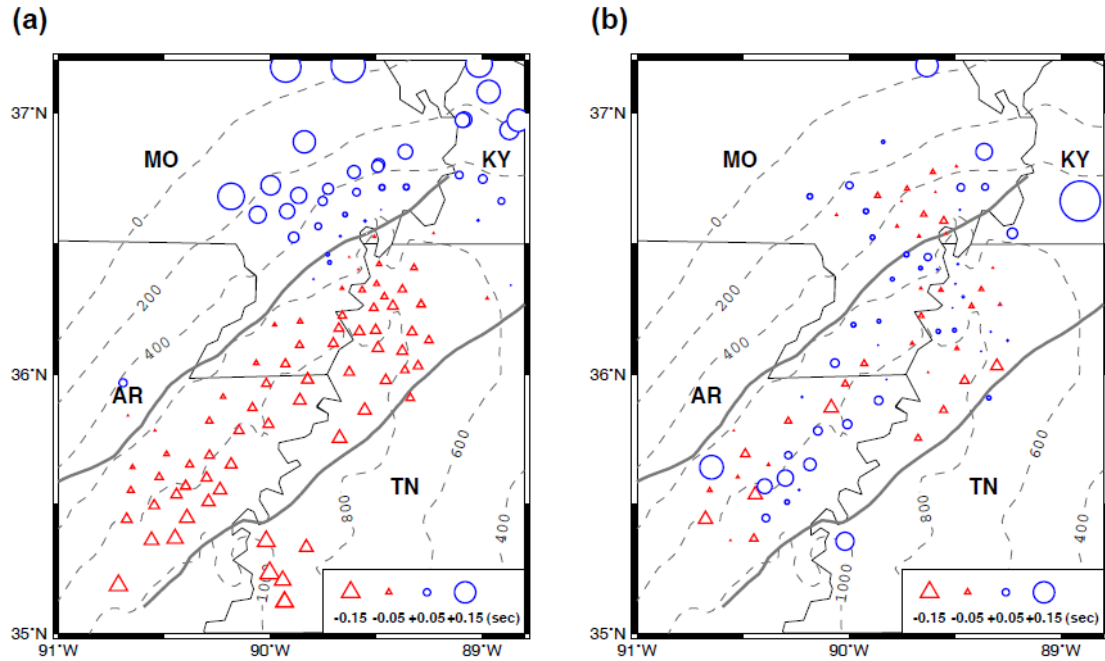


Figure 3.3 Correction terms at each station calculated for station elevation and sediment thickness combined using method M1 (a) and method M2 (b), respectively. The mapped correction terms are relative values to the network mean. Those values will be subtracted from the travel-times before the inversion. Triangles are negative time delays and circles are positive time delays. Two grey thick lines are the boundaries of the Reelfoot rift. Dashed lines are the sediment thickness contours.

These travel-time data were corrected for both station elevation and alluvial sediment thickness in the NMSZ. The latter is necessary because the unconsolidated sediment layer has a very low P wave velocity (1.8 km/sec) (Chiu et al., 1992), and its thickness varies significantly (0–1000 m) in our study area (Figure 3.1), causing a large travel-time variation (up to ~0.5 sec). To correct the effects of the sedimentary cover, we used two independent methods, hereinafter referred to as M1 and M2 (Figure 3.3). Method M1 calculates the correction terms directly by taking Bodin et al.’s (2001) sediment thickness measurements (Figure 3.1) based on hundreds of well logs (Dart, 1992), and assuming vertical ray paths within the sediment layer. The weakness of this method is that

the well-data shortage in some locations may cause biased correction values, especially for where the thickness changes substantially. Method M2 follows Vlahovic et al. (2000) and Vlahovic and Powell’s (2001) idea that the combined correction terms of station elevation and sediment thickness can be replaced by the average station residuals of local phases. This method requires similar sampling ray paths for each station, which in reality is not strictly satisfied. Thus neither method is perfect. Nonetheless, the consistent tomographic results after the two unrelated corrections can be considered “immune” to the sediment effects.

The 1-D initial velocity model for our joint tomographic inversion is listed in Table 3.1. The crust (≤ 40 km) consists of three layers simplified from a crustal model of Chiu et al.’s (1992). The upper mantle (40–160 km) comprises two layers whose velocity values are based on a recent refraction profile (Catchings, 1999). The cell size for our tomography has a fixed horizontal scale of $15 \text{ km} \times 15 \text{ km}$ and a variable vertical scale depending on the initial velocity layers. Slowness in each cell was resolved iteratively by using a nonlinear 3-D tomography method. During the inversion, Laplacian damping was used to balance the resolution and smoothness of the velocity models by trial-and-error. After the inversion, our tomographic models achieved 43.7% and 30.8% variance reductions of travel-time errors from the starting model for the M1 and M2 methods, respectively.

Table 3.1 1-D Initial Velocity Model for Joint Tomographic Inversion

Layers, km	P velocity, km/s
0-5	4.22
5-17	6.17
17-40	6.98
40-100	8.3
100-160	8.4

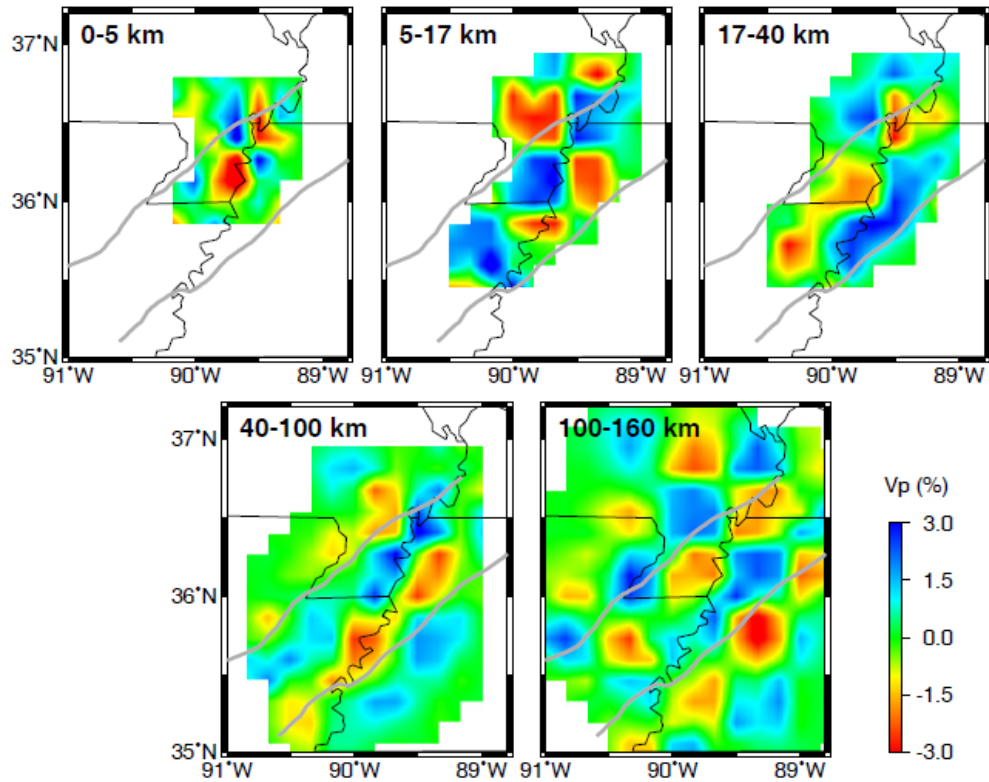


Figure 3.4 A $45 \text{ km} \times 45 \text{ km}$ checkerboard test inverted using the same stations and events for Figures 3.6a and 3.6b. The checkerboard model was synthesized by alternating high and low velocity ($\pm 3\%$) cells. Gaussian noise with a standard deviation of 0.1 sec was added during the inversion.

3.3 Tomography Results

To test the resolution of our inversion, we used a checkerboard model with alternating high and low velocities ($\pm 3\%$) of horizontal scale $45 \text{ km} \times 45 \text{ km}$, and computed synthetic travel-times with the same ray paths as in our real dataset. We then added Gaussian noise with 0.1 sec standard deviation (the root-mean-square of the residuals after the true inversion) to those synthetic travel-times. The inverted tomographic result from the synthetic data is shown in Figure 3.4. Although some smearing occurred in the NE–SW direction due to the uneven distributions of the events and stations, the

alternating patterns were well recovered for most areas. Moreover, a separate sediment leaking test demonstrates that the low-velocity top layer does smear down for our inversion (Figure 3.5).

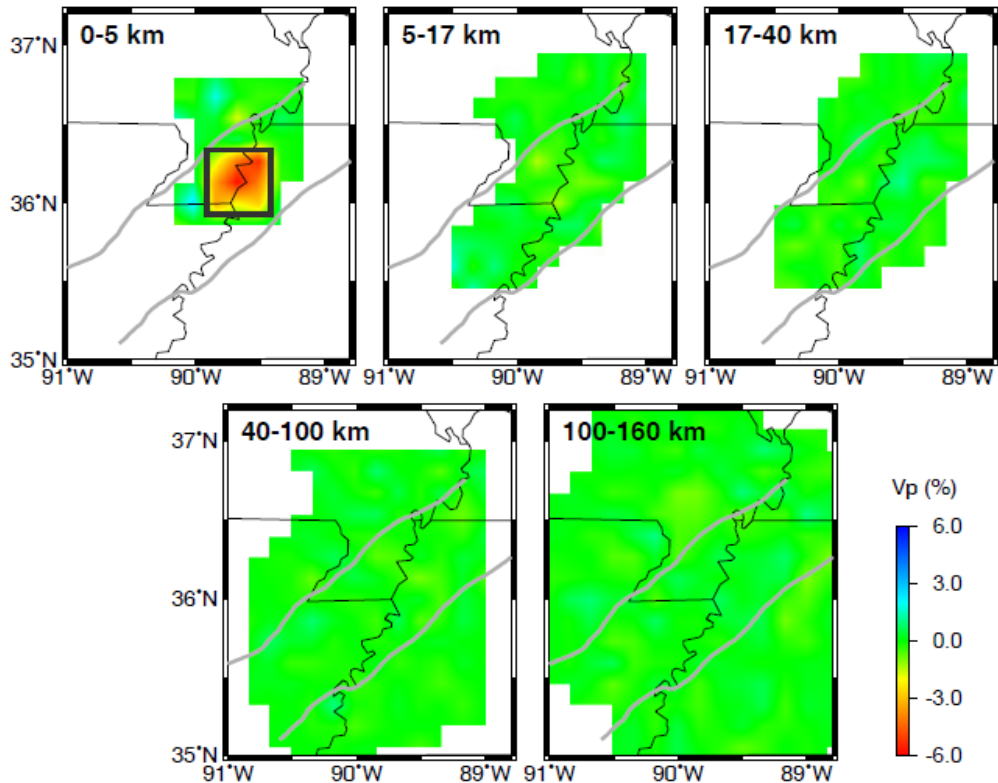
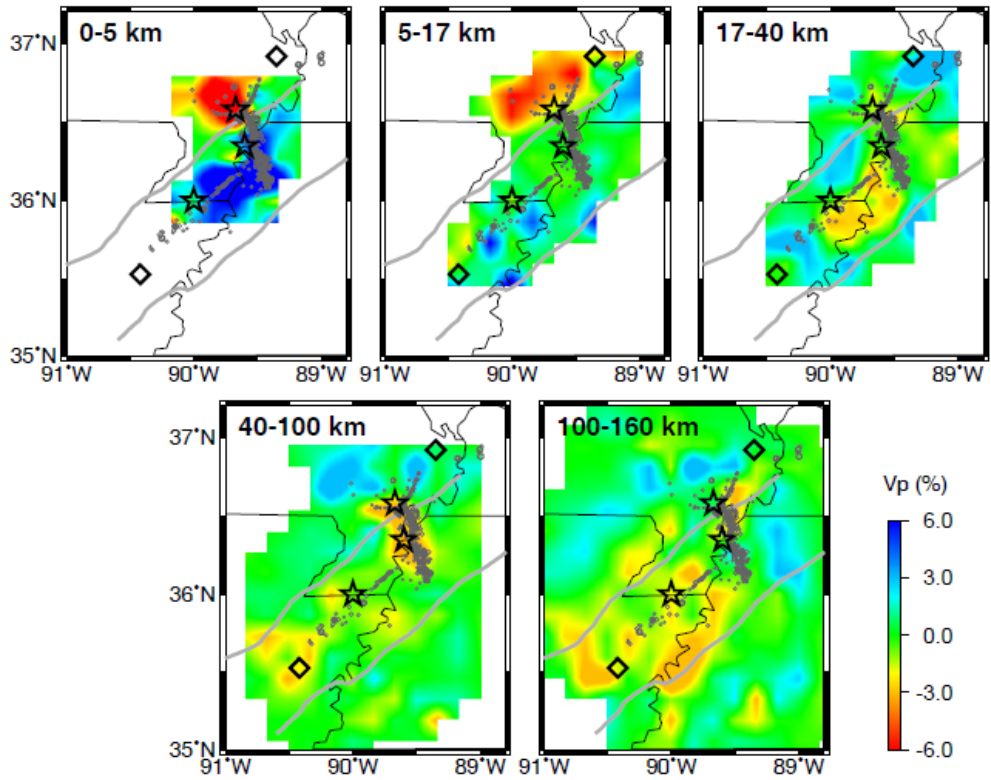


Figure 3.5 Leaking test of the sediment. The test is to check if the low-velocity sediment smears down during the inversion. The sediment is simulated by a $45 \text{ km} \times 45 \text{ km} \times 5 \text{ km}$ uniform low-velocity (-6%) block within the top layer (0-5 km). It is placed at the rectangular box (first figure) within the Reelfoot rift (grey lines). Synthetic travel-times were calculated using the true event-station pairs, then added with Gaussian noise with a standard deviation of 0.1 sec. The inverted tomographic results are shown in five layers (map view). The images demonstrate that the top-layer anomaly is well resolved both horizontally and vertically, and does not leak into the lower crust and mantle. So even though the sediment effects are mistakenly corrected, the deep velocity structures are not significantly affected by the sediment.

(a)



(b)

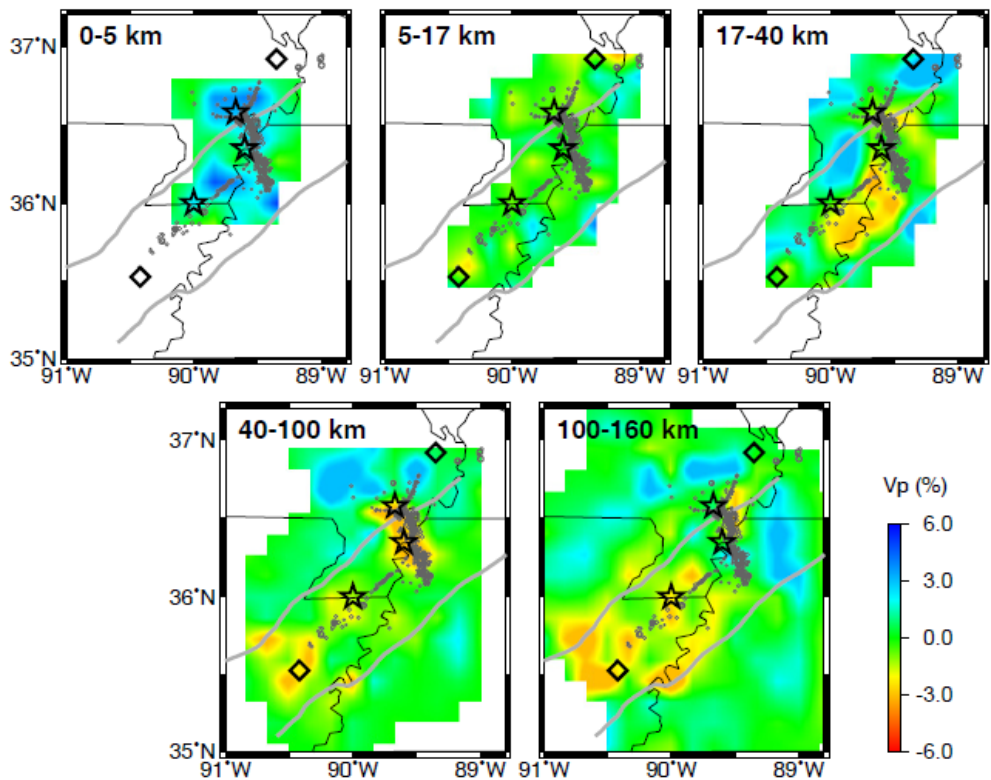


Figure 3.6 (a) Lithospheric P velocity structure for the NMSZ using sediment correction method M1. First P arrivals of 2,056 teleseismic phases and 12,226 local phases were used for the joint inversion. The notions of thick grey lines, stars and diamonds follow Figure 3.1. (b) Counterpart of Figure (a) using sediment correction method M2. Both methods show a low-velocity zone in the lower crust and upper mantle, beneath the seismicity.

Figures 3.6a and 3.6b show the P velocity structures beneath the NMSZ resulting from inverting travel-times with the M1 and M2 corrections, respectively. The major difference is within the upper crust (0–5 and 5–17 km layers), where correction M1 yields a strong low-velocity anomaly to the north of the Reelfoot rift (Figure 3.6a). This could be an artifact introduced by the lack of drill-hole data (Dart, 1992). Furthermore, the anomaly is shallow and beyond the area of our primary interest. Other than for the top two layers, the M1 and M2 corrections produce almost identical velocity images (17–160 km). Therefore the deep structures are not significantly affected by the sediment using our joint dataset. Our analyses will on the features common in Figures 3.6a and 3.6b.

The prime common feature of Figures 3.6a and 3.6b is the low-velocity (up to –3%) zone in the lower crust (17–40 km) and upper mantle (40–160 km). It is spatially associated with three seismic segments in the NMSZ, although its locations vary somewhat from layer to layer. Within the lower crust (17–40 km), the low-velocity anomaly is distributed along the BFZ; for the 40–100 km layer, the low-velocity anomaly is concentrated around the RF and southwestern tip of the BFZ; for the 100–160 km layer, the low-velocity anomaly broadens and covers much of the southwestern Reelfoot rift. The low-velocity zone is surrounded by scattered high-velocity (up to 3%) blocks and primarily confined within the Reelfoot rift, with an overall trend parallel to the rift axis. It also shows a strong spatial relationship with both historic large events and microseismicity.

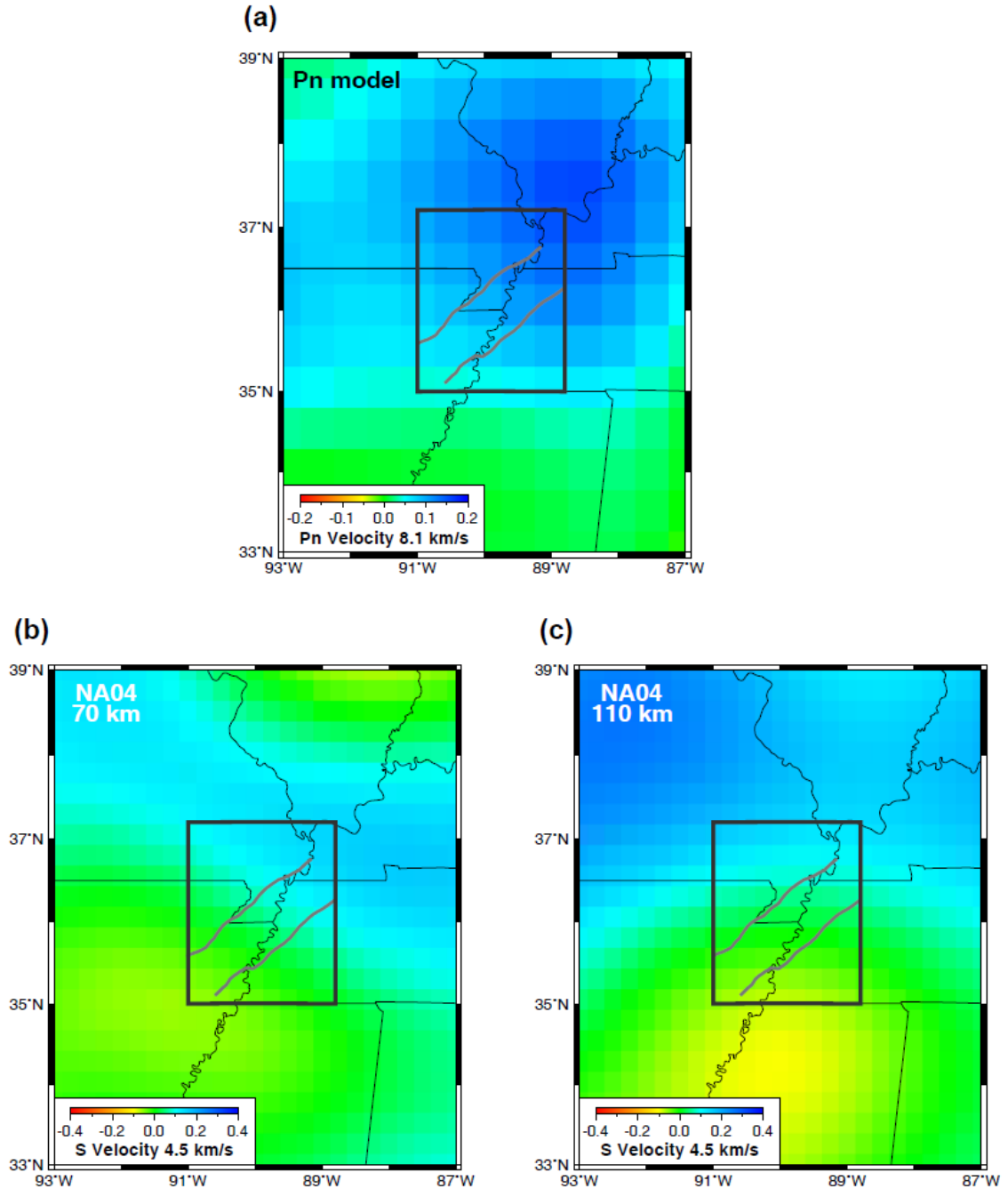


Figure 3.7 Reproductions of the Pn model and the NA04 model in our study and surrounding areas. The inner rectangular box delineates our study area (35°-37.2°N, 88.8°-91°W), and two grey thick lines delineate the boundaries of the Reelfoot rift. (a) Pn wave velocity structure in the NMSZ. The Pn data are provided by Zhang et al. (2009). (b) Shear wave velocity structure of the NA04 model at 70 km in the NMSZ. (c) Counterpart of (b) at 110 km. The data of the NA04 model are provided by Van der Lee and Frederiksen (2005). All these models show that the NMSZ is on the edge of a high-velocity block in the lithosphere.

3.4 Discussion

Our tomographic results are generally consistent with those from previous studies. Vlahovic et al. (2000) used local events to construct the P wave velocity structure in the NMSZ for the top 10.65 km. Their top two layers (<2.65 km) and underlying layers (2.65–10.65 km) show respectively high-velocity and somewhat low-velocity anomalies in the seismic zone, similar to our results. The high-velocity anomaly in the top layer (0–5 km) in our models is consistent with the stable surface indicated by the GPS data (Newman et al., 1999; Calais et al., 2005; Calais and Stein, 2009).

The low-velocity structures we image beneath the Reelfoot rift are similar to those in previous studies using teleseismic P data alone (Mitchell et al., 1977; Al-Shukri and Mitchell, 1987). When incorporating local P data, Al-Shukri and Mitchell's (1987) model shows a belt of slightly higher velocity (up to 1%) in the lower crust of the seismic zone. But the belt is primarily interpolated from the high-velocity data blocks on their model margins. Furthermore, because almost all local events in the NMSZ are too shallow to sample the lower crust, a sufficiently large dataset is needed to resolve the vertical trade-off of delay times. Previous refraction seismic profiles (Mooney et al., 1983; Catchings, 1999) suggest high-velocity intrusions at the bottom of the lower crust, but their interpreted intrusive bodies are broader than the rift zone or the scale of our lower crust image.

Teleseismic tomography inverts relative travel-time residuals and thus only shows relative velocity variations. Regional tomography studies can help constrain the absolute velocity of the study area and understand the context of the NMSZ within the stable North American craton, although their large cell sizes and smoothing may make them unable to resolve small-scale anomalies such as those in our study. Regional surface wave and Pn

tomography models (Van der Lee and Frederiksen, 2005; Zhang et al., 2009) both indicate that the NMSZ is on the edge of a high-velocity block in the upper mantle, with slightly higher absolute velocity (Figure 3.7). Liang and Langston's (2008) ambient noise tomography in the CEUS also shows that the NMSZ is on the western boundary of a high-velocity block for 15 sec period which samples almost the whole crust. The results suggest that the low-velocity anomaly in the NMSZ is a localized feature on the rim of a rigid cratonic root.

The cause of the low-velocity zone in the NMSZ lithosphere is uncertain. The anomaly is localized within the Reelfoot rift and generally follows its trend, and therefore may be genetically linked to the rift. On the other hand, given that the Reelfoot rift initiated in late Precambrian (Ervin and McGinnis, 1975) and the NMSZ lacks clear thermal anomaly (McKenna et al., 2007), the low-velocity anomaly is unlikely to have a thermal origin. Alternatively the low-velocity zone might represent compositional variations across the rift, perhaps related to the magmatism during the Reelfoot rifting. But our results do not favor intrusive bodies in the lower crust because mafic intrusions typically cause high-velocity anomalies within rifts (Mooney et al., 1983). These lead us to speculate that the anomaly is related to the deformational fabrics (weak zone). Although most recent GPS data show little strain rate in the NMSZ and its surrounding area (Newman et al., 1999; Calais et al., 2005; Calais and Stein, 2009), the structural and geometrical analyses suggest that the slip rates of the NMSZ faults could be as high as 4.4–6.2 mm/yr over the last a few thousand years (Mueller et al., 1999; Van Arsdale, 2000). Alternatively, this low-velocity feature could be a preserved weak zone in the lithosphere from the last major tectonic event (e.g., Paleozoic or Mesozoic) within the Reelfoot rift.

The locations of the major intraplate seismic zones in the CEUS (the NMSZ, the East Tennessee Seismic Zone, the Charleston Seismic Zone, and the New England Seismic Zone) are spatially correlated with high-velocity block edges or velocity transition zones in the lithosphere (Liang and Langston, 2008; Zhang et al., 2009). Similar scenarios can be found in other significant intraplate seismic zones such as the Shanxi rift, China (Tian et al., 2009) and the Kutch rift, India (Kennett and Widiyantoro, 1999) which are underlain by a low-velocity zone (presumably a weak zone) bordering a rigid lithospheric root. Those structures suggest that the rheological contrast may play an important role for the intraplate earthquakes. Numerical modelings show that rheological boundaries tend to localize stress near thin lithosphere (Li et al., 2007), and a localized weak zone in the lower crust is likely to shift stress to the upper crust by viscous relaxation. If our lithospheric low-velocity zone in the NMSZ reflects weakness, Kenner and Segall (2000) suggest that such a stress-shifting process can lead to repeated shallow earthquakes. Although present geodetic observations do not detect enough surface motion or strain for large earthquakes (Newman et al., 1999; Calais et al., 2005; Calais and Stein, 2009), it is possible that strain accumulation remains slow during interseismic cycles, especially after large energy is released.

3.5 Conclusions

We have modeled the lithospheric velocity structure of the NMSZ using a combination of teleseismic P and local P travel-time data. Two independent methods correcting for sediment effects yield almost identical velocity variations below the upper

crust. Our tomographic results show that the NMSZ faults are underlain by a localized low-velocity anomaly in the lower crust and upper mantle which is primarily confined within and parallel to the Reelfoot rift. On the other hand, our results do not show compelling evidence for dense mafic intrusions in the lower crust that have been proposed. The low-velocity anomaly under the NMSZ may represent a deep shear zone at rheological boundaries. Such a weak zone could shift stress to the upper crust, thus help explain the repeated earthquakes in the NMSZ where the present-day strain rate is near zero.

3.6 Acknowledgments

We thank Mitchell Withers for providing the waveform data and the CERI catalog and Charles Langston for providing the sediment thickness data. Constructive and detailed comments by an anonymous GRL referee improved this paper. This work was partially supported by the USGS National Earthquake Hazards Reduction Program (NEHRP) grant 04HQGR0046. Qie Zhang acknowledges the Huggins Fellowship support from the University of Missouri.

3.7 References

- Al-Shukri, H.J., and B.J. Mitchell (1987), Three-dimensional velocity variations and their relation to the structure and tectonic evolution of the New Madrid Seismic Zone, *J. Geophys. Res.*, 92, 6377–6390.
- Bodin, P., K. Smith, S. Horton, and H. Hwang (2001), Microtremor observations of deep sediment resonance in metropolitan Memphis, Tennessee, *Eng. Geol.*, 62, 159–168.
- Calais, E., and S. Stein (2009), Time-variable deformation in the New Madrid Seismic

Zone, *Science*, 323, 1442.

Calais, E., G. Mattioli, C. DeMets, J. M. Nocquet, S. Stein, A. Newman, and P. Rydelek (2005), Tectonic strain in plate interiors?, *Nature*, 438, 9–10.

Catchings, R.D. (1999), Regional Vp, Vs, Vp/Vs, and Poisson's ratios across earthquake source zones from Memphis, Tennessee, to St. Louis, Missouri, *Bull. Seismol. Soc. Am.*, 89, 1591–1605.

Chiu, J.M., A.C. Johnston, and Y. T. Yang (1992), Imaging the active faults of the central New Madrid seismic zone using PANDA array data, *Seismol. Res. Lett.*, 63, 375–393.

Dart, R.L. (1992), Catalog of pre-Cretaceous drill-hole data from the upper Mississippi embayment, *U.S. Geol. Surv. Open File Rep.*, 92–685.

Ervin, C.P., and L.D. McGinnis (1975), Reelfoot Rift: Reactivated precursor to the Mississippi Embayment, *Geol. Soc. Am. Bull.*, 86, 1287–1295.

Grana, J.P., and R.M. Richardson (1996), Tectonic stress within the New Madrid Seismic Zone, *J. Geophys. Res.*, 101, 5445–5458.

Hough, S.E., L. Seeber, and J.G. Armbruster (2003), Intraplate triggered earthquakes: Observations and interpretation, *Bull. Seismol. Soc. Am.*, 93, 2212–2221.

Johnston, A.C. (1996), Seismic moment assessment of earthquakes in stable continental regions—III. New Madrid 1811–1812, Charleston 1886 and Lisbon 1755, *Geophys. J. Int.*, 126, 314–344.

Johnston, A.C., and L.R. Kanter (1990), Earthquakes in stable continental crust, *Sci. Am.*, 262, 68–75.

Johnston, A.C., and E.S. Schweig (1996), The enigma of the New Madrid earthquakes of 1811–1812, *Annu. Rev. Earth Planet. Sci.*, 24, 339–384.

Kenner, S.J., and P. Segall (2000), A mechanical model for intraplate earthquakes: Application to the New Madrid Seismic Zone, *Science*, 289, 2329–2332.

Kennett, B.L.N., and S. Widiyantoro (1999), A low seismic wavespeed anomaly beneath northwestern India: A seismic signature of the Deccan plume?, *Earth Planet. Sci. Lett.*, 165, 145–155.

Kennett, B.L.N., E.R. Engdahl, and R. Buland (1995), Constraints on seismic velocities in the Earth from travel times, *Geophys. J. Int.*, 122, 108–124.

Li, Q., M. Liu, Q. Zhang, and E. Sandvol (2007), Stress evolution and seismicity in the

- central-eastern United States: Insights from geodynamic modeling, in *Continental Intraplate Earthquakes: Science, Hazard, and Policy Issues, Spec. Pap. Geol. Soc. Am.*, 425, 149–166.
- Liang, C., and C. A. Langston (2008), Ambient seismic noise tomography and structure of eastern North America, *J. Geophys. Res.*, 113, B03309, doi:10.1029/2007JB005350.
- McKenna, J., S. Stein, and C.A. Stein (2007), Is the New Madrid Seismic Zone hotter and weaker than its surroundings?, in *Continental Intraplate Earthquakes: Science, Hazard, and Policy Issues, GSA Spec. Pap.*, 425, 167–175.
- Mitchell, B.J., C.C. Cheng, and W. Stauder (1977), A three-dimensional velocity model of the lithosphere beneath the New Madrid seismic zone, *Bull. Seismol. Soc. Am.*, 67, 1061–1074.
- Mooney, W.D., M.C. Andrews, A. Ginzburg, D.A. Peters, and R.M. Hamilton (1983), Crustal structure of the northern Mississippi Embayment and a comparison with other continental rift zones, *Tectonophysics*, 94, 327–348.
- Mueller, K., J. Champion, M. Guccione, and K. Kelson (1999), Fault slip rates in the modern New Madrid Seismic Zone, *Science*, 286, 1135–1138.
- Newman, A., S. Stein, J. Weber, J. Engeln, A. Mao, and T. Dixon (1999), Slow deformation and lower seismic hazard at the New Madrid Seismic Zone, *Science*, 284, 619–621.
- Pollitz, F.F., L. Kellogg, and R. Burgmann (2001), Sinking mafic body in a reactivated lower crust: A mechanism for stress concentration at the New Madrid Seismic Zone, *Bull. Seismol. Soc. Am.*, 91, 1882–1897.
- Smalley, R., M.A. Ellis, J. Paul, and R.B. Van Arsdale (2005), Space geodetic evidence for rapid strain rates in the New Madrid Seismic Zone of central USA, *Nature*, 435, 1088–1090.
- Tian, Y., D. Zhao, R. Sun, and J. Teng (2009), Seismic imaging of the crust and upper mantle beneath the North China Craton, *Phys. Earth Planet. Inter.*, 172, 169–182.
- Tuttle, M.P., E.S. Schweig, J.D. Sims, R.H. Lafferty, L.W. Wolf, and M.L. Haynes (2002), The earthquake potential of the New Madrid Seismic Zone, *Bull. Seismol. Soc. Am.*, 92, 2080–2089.
- Van Arsdale, R. (2000), Displacement history and slip rate on the Reelfoot fault of the New Madrid Seismic Zone, *Eng. Geol.*, 55, 219–226.
- VanDecar, J.C., and R.S. Crosson (1990), Determination of teleseismic relative phase arrival times using multi-channel cross-correlation and least squares, *Bull. Seismol.*

Soc. Am., 80, 150–169.

Van der Lee, S., and A. Frederiksen (2005), Surface wave tomography applied to the North American upper mantle, in *Seismic Earth: Array Analysis of Broadband Seismograms*, *Geophys. Monogr. Ser.*, vol. 157, edited by A. Levander and G. Nolet, pp. 67–80, AGU, Washington, D. C.

Vlahovic, G., and C.A. Powell (2001), Three-dimensional S wave velocity structure and V_p/V_s ratios in the New Madrid Seismic Zone, *J. Geophys. Res.*, 106, 13,501–13,513.

Vlahovic, G., C.A. Powell, and J.-M. Chiu (2000), Three-dimensional P wave velocity structure in the New Madrid Seismic Zone, *J. Geophys. Res.*, 105, 7999–8011.

Zhang, Q., E. Sandvol, and M. Liu (2009), Tomographic Pn velocity and anisotropy structure in the central and eastern United States, *Bull. Seismol. Soc. Am.*, 99, 422–427.

CHAPTER 4: RAYLEIGH WAVE TOMOGRAPHY OF THE NORTHEASTERN MARGIN OF THE TIBETAN PLATEAU

Qie Zhang, Eric Sandvol, James Ni, Yingjie Yang, and Yongshun John Chen

Prepared for submission to *Earth and Planetary Science Letters* (2009)

Abstract. The convergence between the more rigid Indian Plate and the relatively weak Eurasian Plate has led to the escape of a large portion of the Tibetan Plateau towards the east-southeast. Various geophysical models have predicted a large-scale flow in both the lower crust and asthenosphere. The escaping continent has also been suggested to move around the rigid and thick lithosphere of the Ordos Plateau and the Sichuan Basin. In order to investigate the path and depth of the continental flow, we have used Rayleigh wave tomography with sensitivity kernels to build both the phase velocity structure (20-143 s) and the shear wave velocity structure (0-200 km) on the northeastern margin of the Tibetan Plateau, using 18 temporary stations deployed for one year as a part of the INDEPTH IV project. From the surface to 100 km, our shear wave velocity model shows a prominent low-velocity anomaly beneath northeastern Tibet, suggestive of a weak lithosphere. In contrast, a high-velocity anomaly exists in our eastern study area, which is consistent with the notion that the Ordos Plateau and the Sichuan Basin are rigid blocks with little internal deformation. The boundary between the high and low velocities lies at $\sim 105^\circ$ longitude and possibly describes the edge of northeastern Tibet. From 125 km to 200 km, our shear wave

velocity model shows a low-velocity channel along the Qilian-Qinling Orogen that is injected into the gap between the Ordos and Sichuan blocks. This channel may be caused by a weak zone associated with the asthenospheric flow, considering that the lithosphere is ~120-150 km thick in northeastern Tibet and the Qinling Orogen. We also inverted for the anisotropy parameters in our study area simultaneously with the velocity parameters. Our dominant fast direction is NNW-SSE, generally consistent with SKS splitting results and the predicted strain from GPS measurements. Furthermore, the fast directions in our anisotropic model do not vary significantly with periods and the anisotropy magnitudes at long periods (100-143 s) are not less than those at short-medium periods (20-80 s), indicating coherent deformation along various depths in our study area and possibly large deformation in the asthenosphere. The deformation seems to be linked to the extrusion tectonics. Lastly, we speculate that the rheological contrast at the edges of the rigid lithospheric blocks plus the strain caused by the east-southeastward extrusion of the Tibet continent is responsible for the intense intraplate seismicity on the northeastern margin of the Tibetan Plateau.

4.1 Introduction

The Tibetan Plateau, the highest topography in the world, is the product of continent-continent collision between the Indian and Eurasian plates that initiated between 50 and 70 My ago (Yin and Harrison, 2000) (Figure 4.1a). The collision has not only lead to significant elevation and highly deformed orogenic belts within the Tibetan Plateau, but also impacted remote areas as far as eastern China and the Baikal rift to the north (Molnar and Tapponnier, 1975; Tapponnier and Molnar, 1977). This well developed

collision zone attracts intense studies, among which is the famous Inter-National Deep Profiling of Tibet and the Himalaya (INDEPTH) project. While the previous three phases of the INDEPTH project focused on the southern and central Tibetan Plateau (e.g., Zhao et al., 1993; Brown et al., 1996; Tilmann et al., 2003), a recent phase IV (2007-2009) of the INDEPTH was designed to investigate the northeastern Tibetan Plateau. As a part of the phase IV, We deployed 18 temporary broadband stations (Figure 4.1b) at the northeastern margin of the plateau from July 2008 to July 2009. The study area connects the Tibetan Plateau with the Ordos Plateau and the Sichuan Basin (Figure 4.1a,b). The latter two belong respectively to the North China block (a part of the Sina-Korea craton) and the South China block (or Yangtze craton) and are separated by the Qinling-Dabie orogenic belt. As a conjunction, our study area is important for us to understand the interactive geodynamics among those three major blocks in China.

The tectonics of the Tibetan Plateau and its adjacent regions is explained by the extrusion theory: as the stronger Indian plate propels the Tibetan Plateau at a rate of ~5 cm/year, the force lead to the lateral escape of the plateau material towards the east-southeast along a series of complicated fault systems (e.g., Molnar and Tapponnier, 1975; Tapponnier and Molnar, 1977). Tapponnier et al. (2001) consider the oblique crustal subduction/thrusting accommodated by the extrusion to be the mechanism of the growth and uplift of the eastern Tibetan Plateau. However, other scholars think that the lower crust flow is responsible for the elevated topography in the eastern plateau (Royden et al., 1997; Clark and Royden, 2000; Clark et al., 2005; Royden et al., 2008). When the escaping continent meets the rigid Ordos and Sichuan blocks, it probably changes directions as indicated by a collection of SKS splitting results (Lev et al., 2006; Chang et

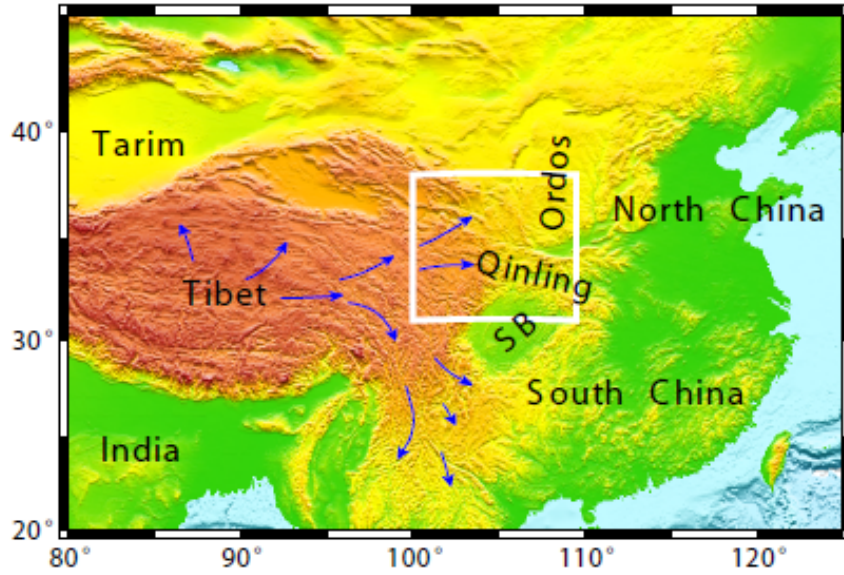
al., 2008; Huang et al., 2008; Wang et al., 2008) (Figure 4.1b). This deformational regime may diverge into two branches wrapping around the Sichuan Basin (Clark and Royden, 2000; Clark et al., 2005; Enkelmann et al., 2006; Royden et al., 2008) (Figure 4.1a). One branch is thought to divert towards the south along the Longmenshan Fault (the western boundary of the Sichuan Basin), joining the south-southeastward movement around the eastern syntaxis (Li et al., 2009). The other branch is believed to squeeze eastward between the Ordos and Sichuan blocks along the Qinling Orogen (Zhang et al., 1998; Huang et al., 2008). However, the tomographic evidences of the proposed flow paths remain unclear.

Another important argument regarding the continental flow hypothesis is the depth extent that it occurs at. Royden and her colleagues propose that the extrusion primarily occurs within the lower crust (Royden et al., 1997; Clark and Royden, 2000; Clark et al., 2005; Royden et al., 2008), considering the insignificant amount of crustal shortening on the eastern plateau margin (Burchfiel et al., 1995). However, other studies (Flower et al., 1998; Liu et al., 2004; Huang et al., 2008) suggest that the extrusion may happen much deeper in the asthenosphere. For example, Liu et al. (2004) imaged low-velocity channels centered at a depth of approximately 250 km that connect western and eastern China using P wave tomography. If the collision-driven lateral extrusion extends to the asthenospheric mantle and into eastern China, Liu et al. (2004) and Huang et al. (2008) believe it could contribute to the widespread rifting and volcanism in eastern China. Some researchers (Flesch et al., 2005; Chang et al., 2008; Wang et al., 2008) advocate coupled deformation between the crust and lithospheric mantle based on the agreement between the shear wave splitting data and the calculated strain field from GPS

observations, but they consider that the lithosphere instead of the asthenosphere is the major source for the observed anisotropy in the Tibetan Plateau.

The earthquake distribution is a third important topic in our study area. The intraplate earthquakes occurred widely in northeastern Tibet and at the edges of the Ordos and Sichuan blocks (Figure 4.1b). Most significant earthquakes are close to 105° longitude. Among them are the catastrophic 1920 Haiyuan ($M\sim 7.8$) and 2008 Wenchuan ($M\sim 7.9$) earthquakes (Figure 4.1b) located near the western boundaries of the Ordos and Sichuan blocks, respectively. The intraplate earthquake distribution may be related to the rheological change in the lithosphere (Zhang et al., 2009a,b) and the regional extrusion tectonics too. To discover the lateral direction and depth extent of the continental flow on the northeastern margin of the Tibetan Plateau as well as the relationship between the lithospheric velocity variations and the seismicity distribution, we investigated the 3-D lithospheric velocity structure in this area using Rayleigh wave tomography. Previous studies primarily focus on the large-scale tomography (e.g., Liu et al., 2004; Huang and Zhao, 2006; Liang and Song, 2006; Pei et al., 2007; Li et al., 2008; Su et al., 2008; Sun et al., 2008), and do not clearly address the detailed velocity structure in our study area. Our Rayleigh surface wave inversion with a sensitivity kernel technique accounts for finite frequency effects, and therefore can provide better resolution. We resolved for both a phase velocity model and a shear wave velocity model in our study area. Shear wave velocities are sensitive to partial melting, so the resolved low-velocity zones may help us image any possible channel of ductile flow in the crust or asthenosphere. A simultaneous inversion resolving for anisotropy along periods was also performed to give an idea about the major deformational directions as a function of depths.

(a)



(b)

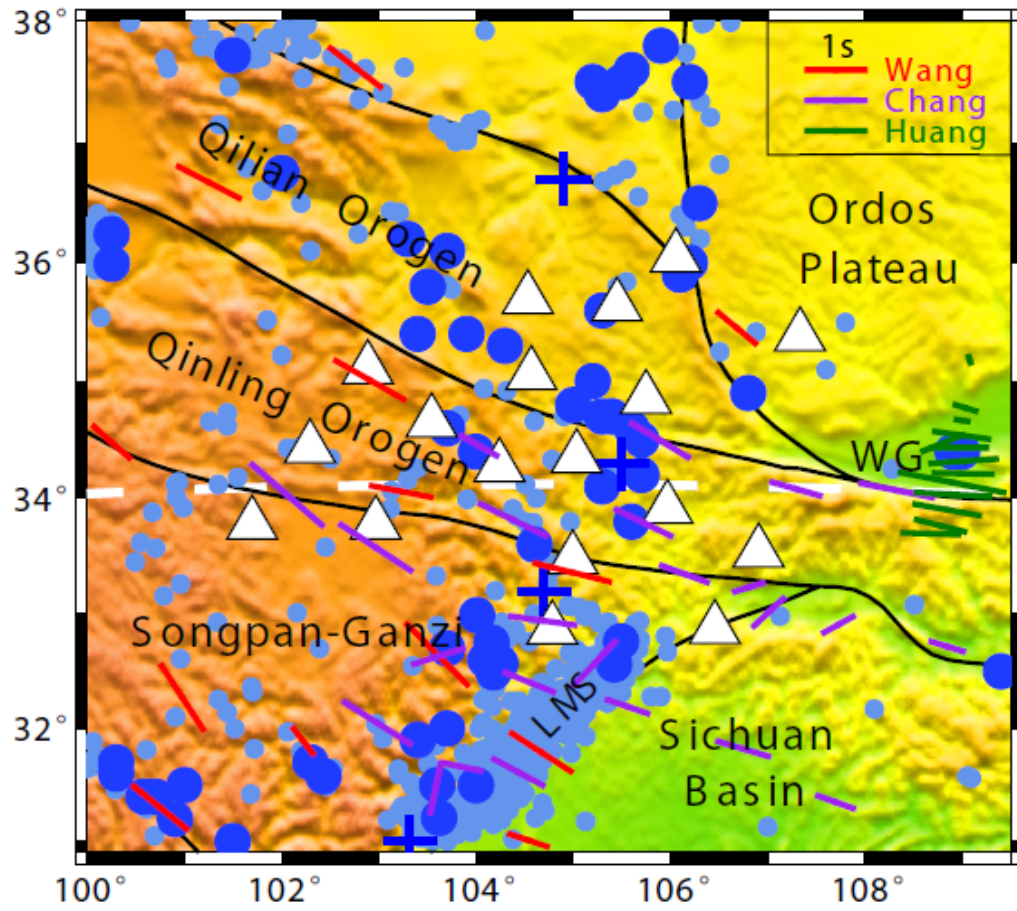


Figure 4.1 (a) Topographic relief of China and the location of our study area (white box). The study area (31° - 38° N, 100° - 109.5° E) is on the northeastern margin of the Tibetan Plateau and includes the western Ordos Plateau and the northwestern Sichuan Basin (SB) that belong to the North China and the South China blocks, respectively. Blue arrows are the escaping directions of lower crust flow from Clark and Royden (2000). (b) Tectonic regions and station distribution in our study area. White triangles denote 18 broadband seismic stations used in this study. The study area is also our inversion area that expands out of the station-covered area. The light and dark blue dots represent both historic and instrument-recorded earthquakes with magnitudes $4.0 \leq M < 6.0$ and $6.0 \leq M < 7.8$, respectively. The blue crosses mark $M \geq 7.8$ earthquakes including the 1920 Haiyuan $M \sim 7.8$ earthquake (36.7° N, 104.9° E) and the 2008 Wenchuan $M \sim 7.9$ earthquake (31.0° N, 103.4° E) that occurred along the Longmenshan Fault (LMS). The red, purple and green bars are the SKS shear wave splitting results from Wang et al. (2008), Chang et al. (2008) and Huang et al. (2008), respectively. The green bars are mostly within the Weihe Graben (WG) that separates the Ordos Plateau from the Qinling Orogen. The dashed white line at 34° N shows the boundary between the northern and southern sub-regions whose anisotropy solutions are plotted in Figure 4.7b and 4.7c, respectively.

4.2 Data Collection and Processing

We utilized fundamental mode Rayleigh waves from teleseismic events for our study. Candidate events were selected using the criteria of (1) magnitude $M_s \geq 5.8$ or $M_b \geq 5.0$, (2) epicenter distance between 25° and 120° , and (3) depth ≤ 100 km. We then carefully examined each individual event and abandoned those with low-quality waveforms. The process yielded a total of 74 good events whose locations are shown in Figure 4.2a. Their azimuths are well distributed, which is important for resolving both lateral velocity heterogeneities and azimuthal anisotropy. The ray coverage is close and excellent for the periods of 40-143 s whose ray numbers are within the range of 820-1000. But the ray numbers decrease gradually to only a few hundred towards the 20 s period. Figure 4.2b-d shows the ray paths at the periods of 25, 50, and 125 s in our study area. The dense crossing ray paths at most periods are ideal for our inversion.

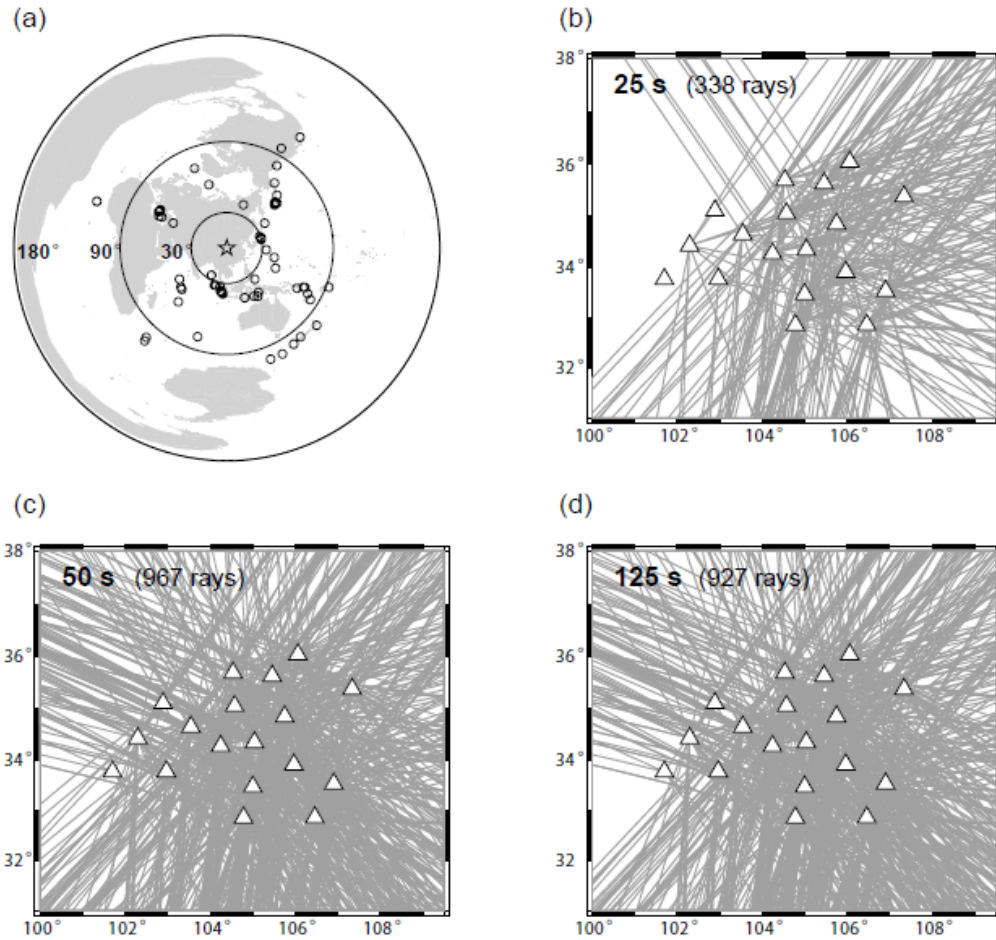


Figure 4.2 (a) Locations of 74 teleseismic events (the circles) used to invert for the Rayleigh wave phase velocities. The star at the map center stands for our study area. Note that the event azimuths are well distributed. (b-d) Great circle ray paths (grey lines) in our study area at the periods of 25, 50, and 125 s, respectively. The ray path coverage within the station network (open triangles) is excellent for 50 and 125 s. Actually, the ray paths for the period range of 40-143 s have close coverage patterns and ray numbers (820-1000 rays).

Our 18 broadband stations consist of all STS2 instruments except for one CMG-3T whose instrument response was converted to STS2 before the following processes. In our study, we have only used the vertical component seismograms of Rayleigh waves to avoid the Love wave interference and the long period noise present on many of the horizontal components. To measure their phase velocities at different

frequencies, we applied to Rayleigh wave signals with 13 band-pass filters that are 10-mHz-wide, zero-phase-shift Butterworth type with center frequencies ranging from 7 to 50 mHz. Each filtered seismogram was manually checked to ensure that only high S/N ratio and coherent waveforms are retained for our tomographic inversion. The signals of fundamental mode Rayleigh waves were then isolated from noise and other phases using a boxcar window with cosine tapers at both ends. The window length is kept identical for all stations given any frequency-event pair. The phases and amplitudes of windowed Rayleigh waves were measured by a Fourier analysis, and the measured amplitudes were normalized for each event to eliminate the influence of the earthquake size.

Other than the energy focusing and defocusing caused by velocity variations, two other categories of major effects on Rayleigh wave amplitudes need to be considered. The first category includes geometric spreading, anelastic attenuation and local/station site response that were corrected according to Yang and Forsyth (2006b). The other is the influence of scattering and multipathing outside the array which is discussed in the following section.

4.3 Methodology

In our study, we used Yang and Forsyth's (2006a,b) method for the Rayleigh wave tomographic inversion. The method is featured by three advantages: (1) using two-plane wave approximation to account for scattering and multipathing, (2) considering both amplitude and phase information, and (3) inverting based on 2-D sensitivity kernels.

Traditional surface wave tomography assumes that the incoming wave travels

along a great-circle path as a plane wave. It usually takes a two-station method to measure the phase differences and further establish a phase velocity model. But lateral heterogeneities between the events and stations can produce strong scattering and multipathing, leading to distorted traveling paths and non-planar wavefields. This phenomenon can be observed from the amplitude variations (or interference) across the network (Forsyth and Li, 2005). Due to this factor, amplitude information is ignored in the traditional method. However, if it is possible to account for the scattering and multipathing effects outside the array which bias the phase velocity solutions within the array, we can take advantage of both amplitude and phase measurements for the inversion. A two-plane wave technique (Li et al., 2003; Forsyth and Li, 2005) helps fix the problem by approximating the incoming wavefield with the sum/interference of two-plane waves. The technique provides stable solutions because it contains only 6 unknown wave parameters, that is, a pair of amplitudes, phases and propagation directions, far fewer than Friederich and Wielandt's (1995) approximation using a set of basis functions. The two-plane wave technique is tested to improve the amplitude and phase misfit by ~30% over one-plane wave technique (Li et al., 2003; Yang and Forsyth, 2006a), and it is widely used for surface wave tomographic studies (e.g., Forsyth et al., 1998; Li et al., 2003; Li and Burke, 2006; Yang and Forsyth, 2006b). We adopted this two-plane wave technique for our study. Considering that the technique may not be suitable for modeling complex wavefields, we down-weighted the input waveform data according to their misfit and removed those with bad misfit.

Another assumption of traditional surface wave tomography is ray theory which is valid only when heterogeneity scales are large enough. Ray theory is not capable of

resolving velocity heterogeneities comparable to the wavelength, because in this situation, the sensitivity of surface waves to the heterogeneities is significant off the ray path. To overcome the limitation and take the finite frequency scattering effects into account, Yang and Forsyth (2006a) developed a method utilizing 2-D sensitivity kernels derived from single-scattering (Born) approximation (Zhou et al., 2004) (in conjunction with two-plane wave technique) for regional surface wave tomography. The sensitivity kernel function primarily focuses in the first two Fresnel zones and shows an overall belly shape with its apex at the station. It provides superior resolution than the previously used Gaussian sensitivity function (e.g., Forsyth et al., 1998; Li et al., 2003; Li and Burke, 2006) which inaccurately assumes constant sensitivity along the ray path and Gaussian-shaped sensitivity orthogonal to the ray path. In their resolution tests with synthetic data, Yang and Forsyth (2006a) demonstrated that their sensitivity kernel method can successfully recover the anomalies greater than or close to the wavelength. The 2-D sensitivity kernel at a given frequency is a function of both the reference phase velocity and the isolation window used for data processing. Here we skip the theory and the mathematical calculation of sensitivity kernels. Refer to Yang and Forsyth's (2006a,b) papers for the details.

Surface wave phase velocity C in a uniformly slightly anisotropic medium depends on both frequency ω and azimuth θ :

$$C(\omega, \theta) = A_0(\omega) + A_1(\omega) \cos(2\theta) + A_2(\omega) \sin(2\theta), \quad (4-1)$$

where A_0 is the azimuthally averaged phase velocity (i.e., isotropic component), A_1 and A_2 are azimuthal anisotropic coefficients, and the high-order terms are neglected

(Smith and Dahlen, 1973). The phase delay $\delta\phi$ and the relative amplitude variation $\delta \ln A$ due to finite frequency scattering effects are defined as:

$$\delta\phi = \iint_{\Omega} K_{\phi}^c(r, \omega) \left(\frac{c - c_0}{c_0} \right) dx^2, \quad (4-2)$$

$$\delta \ln A = \iint_{\Omega} K_A^c(r, \omega) \left(\frac{c - c_0}{c_0} \right) dx^2, \quad (4-3)$$

where $(c - c_0)$ is the phase velocity perturbation, c_0 is the average phase velocity, $K_{\phi}^c(r, \omega)$ and $K_A^c(r, \omega)$ are 2-D phase and amplitude sensitivity kernels, respectively, and the integration area Ω is over the whole study region on the Earth surface.

We parameterized our study area with a total of 300 grid nodes with $0.5^{\circ} \times 0.5^{\circ}$ spacing. It is important to extend our nodes beyond the station-covered area, so it allows the outer nodes to absorb some wavefield effects that are not completely described by two-plane waves. For the same purpose, a larger a-priori error was assigned to the edge nodes than the station-covered nodes during the inversion to permit less constrained solutions at the edge nodes. The phase velocity at any point between the nodes in our study area is expressed by an interpolated value of the velocities at the surrounding nodes using a 2-D Gaussian weighting function. The width L_w of the weighting function plays an important role in balancing the smoothness and resolution of the velocity model. Based on trial-and-error, we chose L_w as 100 km. Other than the parameter L_w , two a-priori variance values serving as damping terms were also assigned to each node in our inversion to control the solutions of velocity and anisotropy, respectively.

Two-stage inversion is adopted in our study to resolve the incoming wavefield

parameters as well as the velocity and anisotropy parameters (A_0 , A_1 and A_2) at each grid node using amplitude and phase data recorded at stations. For the first stage, the velocity model is fixed and only the wavefield parameters are resolved by a simulated annealing method. In the second stage, all of the unknowns including wavefield parameters, velocity and anisotropy parameters, attenuation coefficients, and site responses are resolved based on a standard linear inversion method (Tarantola and Valette, 1982). Typically, the inversion process converges within 10 iterations. More information regarding the inversion is provided by Forsyth and Li (2005) and Yang and Forsyth (2006a,b).

4.4 Results

4.4.1 1-D phase velocity model

Before resolving 2-D phase velocity variations, we need to obtain an initial 1-D velocity model by inverting for the uniform phase velocities in the entire study area. Figure 4.3 shows the calculated average dispersion curve at 13 periods that varies from 3.312 km/s at 20 s to 4.218 km/s at 143 s. Because only one velocity model parameter is resolved for each period, the solutions are well constrained with very small standard deviations (0.004-0.008 km/s). The dispersion curve shows a consistent shape of concave downward, indicating non-existence of a low-velocity zone. A slope change at 33-50 s or ~40 s may correspond to the crust-mantle transition, where the surface wave sensitivity range shifts from both crust and mantle to mainly mantle.

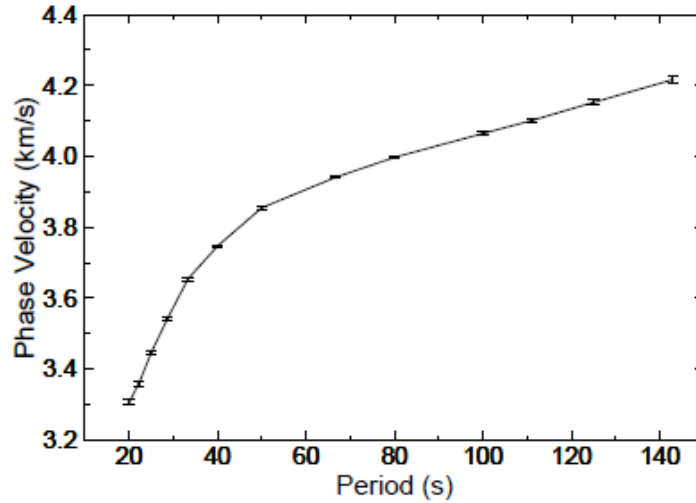


Figure 4.3 Average Rayleigh wave phase velocities in our study area at 13 periods ranging from 20 to 143 s. This 1-D dispersion curve is used as an initial model for the inversions of 2-D phase velocity model (Figure 4.4) and 1-D shear wave velocity model (Figure 4.5). Error bars show the two standard deviations from the mean.

4.4.2 2-D phase velocity model

Using the above initial velocity model, we inverted for the lateral variations of isotropic phase velocities (A_0 in equation (4-1)) at each grid node for different periods. For the plotting purpose, we interpolated the phase velocities at finer grids ($0.05^\circ \times 0.05^\circ$) by using the same Gaussian weighting function ($L_w = 100$ km). The interpolated velocity maps are actually identical to those measured during the inversion. Figure 4.4a-k shows the result of the 2-D phase velocity model at the periods of 20, 25, 33, 40, 50, 67, 80, 100, 111, 125, and 143 s. Rayleigh wave phase velocities at different periods reflect the integrated shear velocity information over different depth ranges with the maximum sensitivity at the depth of $\sim 1/3$ wavelength. Due to the overlaps of sampling depths, the phase velocity maps show gradual changes among adjacent periods.

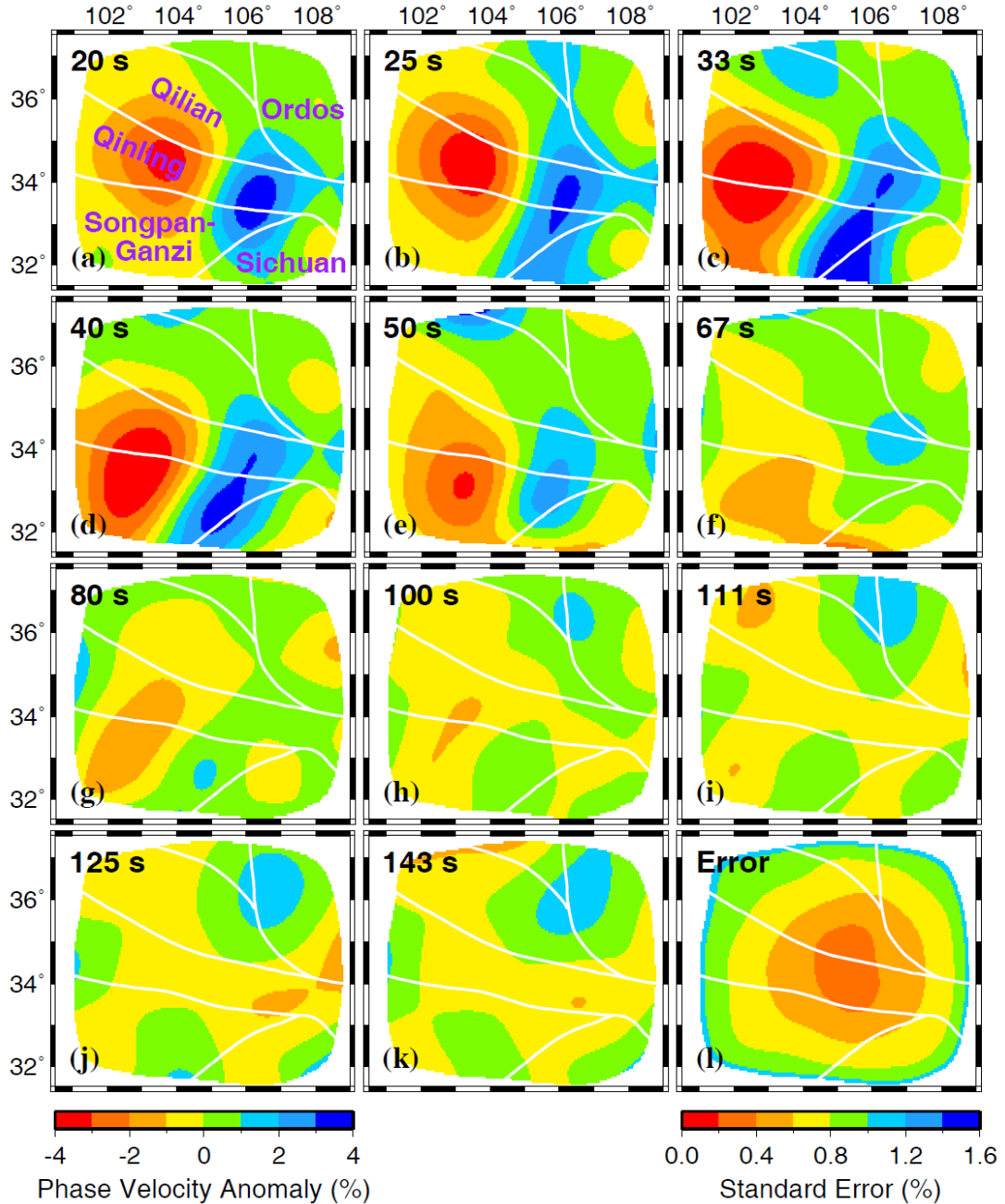


Figure 4.4 Maps of 2-D isotropic Rayleigh wave phase velocities (a-k) and the phase velocity uncertainties at 50 s (l). We resolved the lateral phase velocity variations at 13 periods ranging from 20 to 143 s. Eleven of them are displayed here: (a) 20 s, (b) 25 s, (c) 33 s, (d) 40 s, (e) 50 s, (f) 67 s, (g) 80 s, (h) 100 s, (i) 111 s, (j) 125 s, and (k) 143 s. Note that the plotting area (31.5° - 37.5° N, 100.5° - 109° E) is slightly smaller than the inversion area in Figure 4.1b. Velocity perturbations are calculated relative to the average phase velocities shown in Figure 4.3. The poorly constrained edge areas of the velocity maps are masked by the 1.0% standard error contour at 50 s (l). Actually, the error maps at the period range of 40-143 s are very close because the ray paths at those periods are similar. The white lines are the tectonic boundaries as in Figure 4.1b.

The average crust thickness in our study area is ~50 km (see the discussion in the next section). The 20-33 s Rayleigh waves have the maximum sensitivity at the depths of ~22-40 km and primarily sample the crust velocity variations. The major feature is the low-velocity Tibet on the west and the high-velocity structure on the east, with a velocity contrast up to 8%. The sharp boundary at ~105° longitude seems to delineate the northeastern edge of the Tibetan Plateau. For the periods of 40-67 s, the largest sensitivity of the Rayleigh waves varies from the depth of ~50 km to ~88 km. As the maximum sensitivity depths shift from the lower crust to the lithospheric mantle, the amplitudes of both low-velocity and high-velocity anomalies decrease, with their boundary still fixed at ~105° longitude. The velocity pattern changes at high periods. At the periods of 100-143 s, whose greatest sensitivity occurs at ~136-201 km, a low-velocity (up to 1%) channel along the Qilian-Qinling Orogen appears. It penetrates the gap between the Ordos Plateau and the Sichuan Basin, and connects the west with the east.

The standard errors of phase velocities at different periods are estimated from the model covariance matrices and the weighting function. All of these standard error maps share a similar pattern with error values increasing from the center (station-covered area) to the edge of the study area. An example of standard error map at 50 s period is shown in Figure 4.4l. Actually, the error maps at the periods of 40-143 s are very close because of the similar ray paths and coverage at those periods (Figure 4.2b-d). The 1.0% error contour in Figure 4.4l is used to mask the poorly constrained edge areas of our 2-D phase velocity model (Figure 4.4a-k).

4.4.3 1-D shear wave velocity model

For the purpose of geological interpretation, we need to convert the phase velocities to the shear wave velocities, so the velocity information for a given depth range can be isolated. Rayleigh wave phase velocities rely majorly on S wave velocities, instead of P wave velocities and density. Therefore we can assume a constant Poisson's ratio and only invert for the S wave velocity structure. During the inversion, Saito's (1988) algorithm is used to calculate the partial derivatives of phase velocities with respect to model parameters (i.e., P and S wave velocities) and the synthetic phase velocities that best fit the real phase data. Because the inversion process is non-linear and underdetermined, we assigned a-priori constraints, that is, a correlation coefficient and a standard error value to the diagonal and off-diagonal components of the model covariance matrix, respectively, to allow damping and vertical smoothing during the inversion. The average shear wave velocity model in our study area is first resolved to serve as an initial model for the next step of 3-D inversion.

Due to the large tradeoff between the Moho depth and the seismic velocity structure adjacent to the Moho discontinuity, we took the a-priori information of crust thickness for our 1-D inversion. Receiver function studies (Li et al., 2006b; Duan et al., 2007; Tong et al., 2007; Lou et al., 2009) suggest an average Moho depth at ~50 km in our study area (Figure 4.6i). Li et al.'s (2006b) stations cover a large part of our central study area with the Moho depths varying from 44 km to 56 km. Duan et al.'s (2007) receiver function analysis on a N-S array of 22 stations at ~103° longitude yields an approximately flat Moho at 50 km. Tong et al.'s (2007) 13-station array crossing the southwestern edge of the Ordos Plateau produces close crust thickness values (49-55 km)

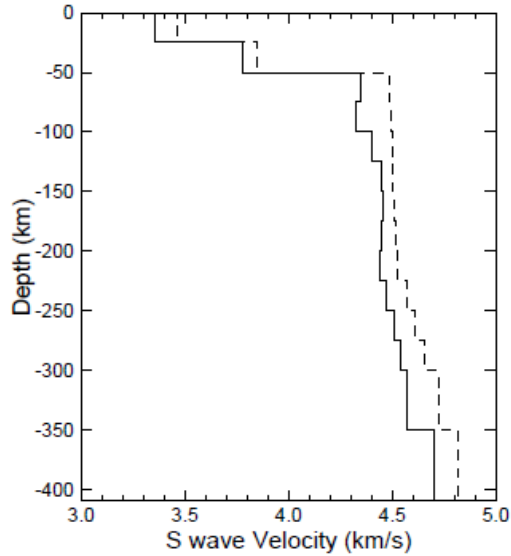


Figure 4.5 Average shear wave velocities (solid line) in our study area. This model is obtained by inverting average phase velocities in Figure 4.3 with the crust thickness fixed at 50 km. The starting model for the inversion is a slightly modified AK135 velocity model (dashed line). The resolved 1-D shear wave velocities are lower than the AK135 reference velocities. Our resolved 1-D model is then adopted as an initial model for the 2-D inversion of shear wave velocities (Figure 4.6).

with a mean of 52 km. Lou et al.'s (2009) study shows that the Moho depths change from 40 km in the western Sichuan Basin to 56 km in the Songpan-Ganzi terrane. Other than the receiver function results, a summation of deep seismic sounding data in China (Li et al., 2006a) gives ~50 km of the average Moho depth in our study area as well. Therefore we fixed the crust thickness at 50 km for our 1-D shear wave velocity inversion. We slightly modified the AK135 model (Kennett et al., 1995) to create our 1-D initial model which primarily contains 25-km-thick layers. During the inversion, it is reasonable to allow the 1-D velocities to vary down to 410 km because the average velocities are well constrained. The result is shown in Figure 4.5, where we can see the resolved average shear wave velocities are smaller than those in the reference AK135 model. It suggests that partial melting may occur widely in our study area.

4.4.4 3-D shear wave velocity model

We obtained our 3-D shear wave velocity model by applying the previous 1-D inversion method (section 4.4.3) to each map point in our study area. During the inversion, the shear wave velocities are fixed below 200 km where Rayleigh wave data do not have sufficient resolution to determine the lateral velocity variations reliably. The initial model for the map point inversion is our optimal 1-D model (Figure 4.5) with its crust thickness corrected according to the interpolated/extrapolated Moho depths from receiver function analyses (Li et al., 2006b; Duan et al., 2007; Tong et al., 2007; Lou et al., 2009) (Figure 4.6i). The corrected Moho depths vary from 40 km to 56 km in our study area, and the upper crust thickness is defined to be half of the Moho depth. Again, both upper crust and lower crust thicknesses are fixed during the map point inversion.

It is important to note that the Moho depths vary dramatically and abruptly in our study area (Figure 4.6i), and the resolved shear wave velocity structure adjacent to the Moho discontinuity is highly depending on the crust thickness values specified in the initial models. Due to the limited constraints from the available receiver function data, the resolved small velocity anomalies around the Moho could be artifacts due to potential errors in our a-priori crust thickness map. Therefore, we only interpreted the first-order features in the first 100 km of the resolved velocity model. We have tested our 3-D shear wave velocity model by using different Moho depth maps including Li et al.'s (2006a) Moho map as well as a flat 50 km Moho map, but found that the resolved structures beneath 100 km are only slightly affected by the choices of the crust thickness maps.

The results of 3-D shear wave velocities are shown in Figure 4.6a-h with a similar pattern to our phase velocity maps (Figure 4.4a-k). For the depths of 0-100 km, the

first-order feature of the shear wave velocity model is still the low-velocity (up to -4%) northeastern Tibet and the high-velocity (up to 3%) eastern study area. The major

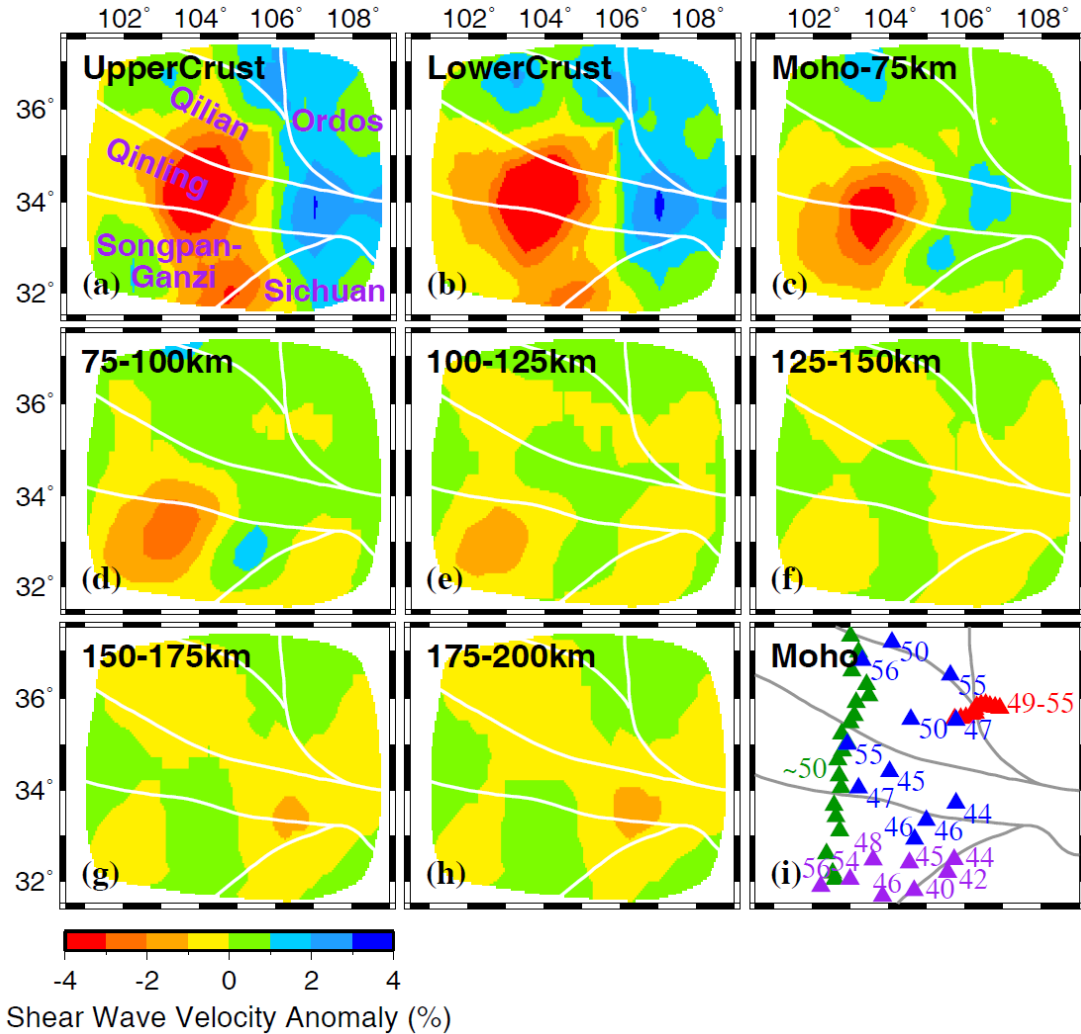


Figure 4.6 Maps of 2-D isotropic shear wave velocities (a-h) and Moho depths (i) in our study area. The shear wave velocity model is constructed by inverting the dispersion curve at each map point. The shear wave velocities at 0-200 km are resolved with the rest fixed during the inversion. The initial model for the inversion is adopted from Figure 4.5 with the Moho depth corrected according to the receiver function results (i). Figure (a) layer (upper crust) is from the surface to half of the Moho depth. Figure (b) layer (lower crust) is from half of the Moho depth to the Moho depth. Figure (i) shows the Moho depths from the receiver function analyses. Red, green, blue and purple triangles stand for the stations from Tong et al. (2007), Duan et al. (2007), Li et al. (2006b) and Lou et al. (2009), respectively. The adjacent numbers are Moho depths in kilometers.

difference between the phase and shear wave velocity models is the high-velocity anomaly shifted eastwards in the latter model. For the depths of 125-200 km, the shear wave velocity model still indicates a low-velocity (up to -1%) channel along the Qilian-Qinling Orogen existing between the Ordos and Sichuan blocks, similar to our phase velocity model. Since our average shear wave velocities at 125-200 km are 1-1.5% lower than those of the global AK135 model (Figure 4.5), the low-velocity channel may be up to 2.5% lower than the global average velocity.

4.4.5 1-D anisotropy model

Unlike shear wave splitting measurements characterized by poor vertical resolution, the anisotropy analysis using surface waves provides valuable vertical information because surface waves are sensitive to different depth ranges at different periods. To find the azimuthal anisotropy features of Rayleigh waves at those 13 periods in our study area, we performed another inversion simultaneously resolving for the velocity coefficient A_0 and the anisotropy coefficients A_1 and A_2 in equation (4-1). The percentage of anisotropy magnitude (the difference in the velocities between the fast and slow directions divided by the isotropic velocity) is then measured by the formula $2\sqrt{A_1(\omega)^2 + A_2(\omega)^2} / A_0(\omega)$. The fast direction θ (anisotropic azimuth) is calculated by either $\frac{1}{2} \tan^{-1}(A_2(\omega) / A_1(\omega))$ or $\frac{1}{2} \tan^{-1}(A_2(\omega) / A_1(\omega)) + \frac{\pi}{2}$ that maximizes the $C(\omega, \theta)$ value in equation (4-1). Standard deviations of the magnitude and fast direction can further be estimated from the variances of A_1 and A_2 using an error propagation

technique (Clifford, 1975). Although anisotropy terms are introduced, the resolved velocity image is very close to the result (section 4.4.2 and Figure 4.4) after the inversion with only isotropic terms. The fact is probably due to the even azimuthal coverage of our ray paths.

Theoretically, 2-D anisotropy can be resolved at each grid node, but this nearly triples the number of unknowns during the inversion that can cause instability in our solutions. In order to test the stability of our anisotropy models, we performed two inversions. First, we resolved for the uniform azimuthal anisotropy in the whole study area that varies only with periods (Figure 4.7a). The result shows a consistent NNW-SSE fast direction for all the periods and increasing anisotropy amplitudes from $\sim 1\%$ at 22-80 s to $\sim 3\%$ at 100-143 s. For the second inversion, we divided the study area into only two sub-regions because of the limited station number. Each sub-region is assumed to be uniformly anisotropic. We tested on a series of different division boundaries that split the study area into western and eastern sub-regions, or northern and southern sub-regions. The results show that a splitting line at 34° latitude (Figure 4.1b) yields stable and coherent solutions. The resolved anisotropy parameters for the northern and southern study areas are plotted in Figure 4.7b and 4.7c, respectively. The northern sub-region still demonstrates a consistent NNW-SSE fast direction (Figure 4.7b), as the first inversion does (Figure 4.7a), but it has a different pattern of amplitudes that are all strong (2-3%) and close in values. On the contrary, the southern sub-region is featured by weak anisotropy ($< 1.5\%$) for all the periods (Figure 4.7c). The anisotropy at the periods of 20-50 s shares a common NE-SW fast direction (with the amplitudes of $\sim 1\%$) which is approximately orthogonal to the fast direction in Figure 4.7a and 4.7b. The anisotropy

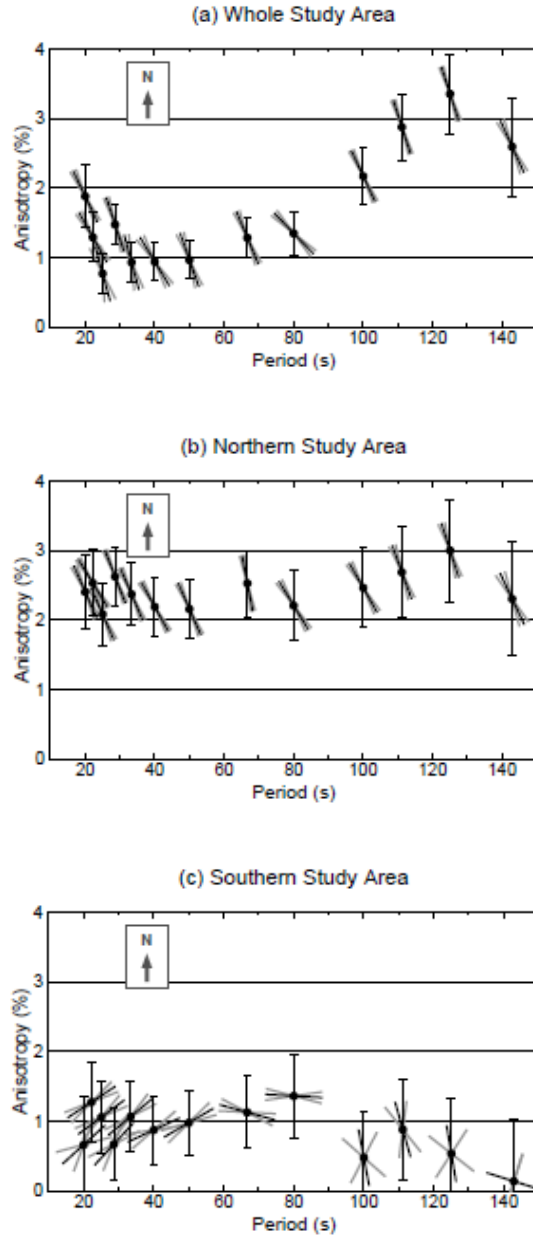


Figure 4.7 Variations of average azimuthal anisotropy with periods in the whole study area (a), the northern study area (b), and the southern study area (c). The result (a) was resolved by assuming uniform anisotropy in the whole study area that varies only with periods. The results (b) and (c) were resolved simultaneously in another inversion by splitting the whole study area into two sub-regions with a boundary at 34° latitude (dashed white line in Figure 4.1b). Each sub-region is assumed to be uniformly anisotropic. For each period in Figures (a), (b) and (c), the percentage of anisotropy magnitude is represented by the vertical axis, and the fast direction of azimuthal anisotropy is represented by the orientation of a slanted black bar as in a map view with North pointing up. One standard deviations of the anisotropy magnitude and fast direction are depicted by a pair of vertical and slanted grey bars, respectively.

orientation then changes to nearly W-E at 67 and 80 s. At higher periods (100-143 s), the anisotropy becomes very weak ($< 1\%$) and not well constrained, but its fast directions generally agree with Figure 4.7a and 4.7b. Based on the two inversions, we can tell that our anisotropy originates largely from the northern study area, and the magnitudes of dominant anisotropy at high periods are equal or larger than those at low-medium periods. Based on the observations of coherent anisotropy changes along periods and small fast direction error bounds in both Figure 4.7b and 4.7c, we propose a distinct change in the anisotropic fabrics at 34° latitude or at the location of the Qinling Orogen.

4.5 Discussion

Both our 2-D phase velocity model (Figure 4.4) and shear wave velocity model (Figure 4.6) reveal some interesting anomalies within our study area. The patterns of the velocity variations fall into two categories: (1) short periods (20-67 s) or 0-100 km; (2) long periods (100-143 s) or 125-200 km. According to An and Shi (2007), the lithosphere thickness beneath the northeastern Tibetan Plateau and the Qinling Orogen is ~ 120 -150 km. So the velocity pattern change may be related to the transition from the lithosphere to the asthenosphere in our study area.

The phase velocity maps at the periods of 20-67 s (Figure 4.4a-f) show a prominent low-velocity (up to -4%) anomaly beneath the northeastern Tibetan Plateau with a boundary at $\sim 105^\circ$ longitude. The same low-velocity (up to -4%) zone also appears in the shear wave velocity maps from surface to 100 km (Figure 4.6a-d). The northeastern Tibetan Plateau is dominated by highly deformed orogenic belts and fold zones (the

Qilian Orogen, the Qinling Orogen, and the Songpan-Ganzi fold zone), and the associated low-velocity anomaly may present weak crust and lithosphere. The continental flow has also been proposed to occur broadly in this low-velocity area (Royden et al., 1997; Clark and Royden, 2000; Clark et al., 2005; Royden et al., 2008; Flesch et al., 2005; Chang et al., 2008; Wang et al., 2008). On the contrary, our eastern study area including the Ordos Plateau and the Sichuan Basin shows fast velocities in the lithosphere (0-100 km). The phase velocity maps at the periods of 20-67 s (Figure 4.4a-f) image the highest velocity (up to 4%) anomaly next to the boundary of northeastern Tibet, i.e., from the Longmenshan Fault to the southwestern edge of the Ordos Plateau. This anomaly primarily reflects the crust structure because both its size and amplitude decrease dramatically at 50-67 s (Figure 4.4e-f) whose largest sensitivity shifts to the depths (~64-88 km) below the Moho. According to the receiver function results (Li et al., 2006b; Duan et al., 2007; Tong et al., 2007; Lou et al., 2009) (Figure 4.6i), the shallowest Moho matches the highest-velocity anomaly in our study area, so the anomaly is most likely caused by sampling more mantle structures compared to where the Moho is deeper. The influence of the Moho depths to the phase velocities is also demonstrated by the fact that this pronounced high-velocity anomaly becomes damped or shifted (Figure 4.6a-d) when converted to the shear wave velocities. When taking the crust thickness into account, the highest shear wave velocity anomaly is shifted eastwards for the depths of 0-100 km (Figure 4.6a-d). The Ordos Plateau and the Sichuan Basin are overall featured by high lithospheric velocities because they are old and stable blocks with little deformation and few earthquakes (Figure 4.1b). As a summary for the lithospheric structure, we observed a clear velocity boundary at $\sim 105^\circ$ longitude that splits the low-velocity northeastern

Tibet from the high-velocity Ordos and Sichuan blocks. The same lithospheric velocity pattern has also been imaged by many other tomographic studies using Pn and Sn waves (Liang and Song, 2006; Pei et al., 2007), P waves (Huang and Zhao, 2006; Li et al., 2008), S waves (Sun et al., 2008), Rayleigh waves (Su et al., 2008), and ambient noise surface waves (Li et al., 2009), although their study areas are much larger or vary somewhat from ours.

The phase velocity pattern at the periods of 100-143 s (Figure 4.4h-k) changes from that at short periods. The long period maps show a low-velocity (up to -1%) channel along the Qilian-Qinling Orogen that connects the western study area with the eastern study area. The channel seems to be bounded by the high-velocity blocks of the Ordos Plateau and the Sichuan Basin. It keeps the similar shape in our shear wave velocity model that spans the depths of 125-200 km (Figure 4.6f-h). The low-velocity channel is also observed at 200-300 km in large-scale P wave velocity models (Liu et al., 2004; Huang and Zhao, 2006; Li et al., 2008). Given the deep lithospheric roots of the Ordos and Sichuan blocks (Huang and Zhao, 2006; Pei et al., 2007), the gap between them is likely to serve as an ideal passage for the escaping flow as the continental material is pushed eastwards. Our results indicate that the injection of the low-velocity material between the Ordos and Sichuan blocks starts at 125 km and extends to the bottom of our model. Although our tomography does not provide sufficient resolution below 200 km, other tomographic studies show that the W-E trending low-velocity channel becomes massive beneath 300 km, even expanding the Ordos Plateau and the Sichuan Basin (Liu et al., 2004; Huang et al., 2006; Li et al., 2008). The low-velocity channel is suggestive of a deep ductile flow eastward in the asthenosphere, but for further confirmation, we need

the constraints from the anisotropy data to see if the corresponding deformation indeed exists.

Figures 4.7a-c show that the anisotropy in our study area can be divided into the northern and southern sub-regions along the Qinling Orogen. The prevailing shear wave polarization direction is NNW-SSE and primarily contributed from the northern study area above 34° latitude. The polarization direction generally agrees with those from a Rayleigh wave anisotropy study (Su et al., 2008), SKS splitting analyses (Chang et al., 2008; Wang et al., 2008), and the predicted strain (Flesch et al., 2005; Wang et al., 2008) from GPS measurements. The consistency plus the fact that our dominant fast direction (NNW-SSE) does not vary with periods (Figure 4.7a,b) indicates vertically coherent deformation. The deformation is likely linked to the continental flow southeastward caused by the escape tectonics. Our southern study area yields small anisotropy for all the periods that splits into two polarization trends (Figure 4.7c): the NE-SW and W-E fast directions for short-medium periods (20-80 s) that deviate from the dominant NNW-SSE direction, and the NNW-SSE fast direction for long periods (100-143 s) whose anisotropy amount (~0.5%) is within our error estimates. Chang et al.'s (2008) SKS splitting data also indicate complicated fast directions including both NE-SW and NW-SE orientations in this sub-region. Our weak and multi-orientated anisotropy in the southern area is probably caused by the obstacle of the Sichuan block with its western boundary almost perpendicular to the dominant extrusion direction.

The Qinling Orogen is the collision boundary between the North China and South China blocks, and the SKS splitting results (Chang et al., 2008; Hang et al., 2008; Wang et al., 2008) show strike-parallel fast directions along the Qinling (Figure 4.1b). Although

the lithospheric deformation caused by the collision may explain the anisotropy orientation, Huang et al. (2008) conclude that the asthenospheric deformation needs to contribute largely because the Qinling lithosphere (≤ 150 km thick) alone does not account for some extra-large delay times (≥ 1.8 s). Huang et al. (2008) further propose that the most likely candidate for the large anisotropy is the asthenospheric flow along the Qinling channel produced by the extrusion tectonics. This is consistent with the imaged asthenospheric low-velocity channel along the Qilian-Qinling Orogen in our tomographic results. So it is likely that as the extruded continent moves towards east-southeast, some in the asthenosphere indeed passes eastwards through the gap between the Ordos and Sichuan blocks. The anisotropy mechanism beneath the Sichuan Basin and its western boundary is not clear, because our anisotropy model and the SKS splitting data both show two different fast directions with one orthogonal to the other.

Different hypotheses have been proposed regarding the depth extent that the escaping flow occurs at. Roydon et al. (Royden et al., 1997; Clark and Royden, 2000; Clark et al., 2005) suggest that the extrusion is accommodated by the ductile flow primarily confined within the lower crust. However, the shear wave splitting data and the predicted strain field from GPS observations are very consistent in our study area, indicating coherent deformation between the crust and mantle (Flesch et al., 2005; Chang et al., 2008; Wang et al., 2008). During a test where the asthenospheric deformation was introduced, Flesch et al. (2005) found a large misfit for the resolved anisotropy model using the SKS splitting and surface deformation data, so they advocate that the anisotropy is dominantly lithospheric in the Tibetan Plateau. However, our anisotropy model (Figure 4.7a) shows a uniform dominant NNW-SSE fast direction for all the periods (20-143 s),

and the anisotropy amplitudes at long periods are at least as large as at short periods. This fact reflects consistent deformation in our study area from the crust to the depth of 200 km which is probably caused by the escape tectonics. Because the lithosphere in the northeastern Tibetan Plateau is ~120-150 km thick (An and Shi, 2007), the strong anisotropy (~2.7%) at 100-143 s in our model (Figure 4.7a,b) is suggestive of a significant portion of anisotropic fabrics in the asthenospheric mantle. Huang et al.'s (2006) and Chang et al.'s (2008) shear wave splitting analyses also record a few large delay times that are no less than 1.8 s and 1.4 s, respectively (Figure 4.1b), which require the existence of the asthenospheric deformation.

Last, our velocity model may explain some aspects of the intense intraplate earthquakes in our study area. Numerous earthquakes occurred on the margins of and to the west of the Ordos Plateau and the Sichuan Basin that are old and rigid blocks with little interior seismicity (Figure 4.1b). Most significant intraplate earthquakes are located close to 105° longitude, including the catastrophic 1920 Haiyuan (M~7.8) and 2008 Wenchuan (M~7.9) earthquakes. This most active seismic zone matches our lithospheric velocity boundary at ~105° longitude that separates the low-velocity northeastern Tibet from the high-velocity Ordos and Sichuan blocks (Figure 4.1b). Studies on the major intraplate seismic zones in the eastern United States (Zhang et al., 2009a,b) suggest that the lithospheric structure is the key to understand the intraplate seismicity where the theory of plate tectonics does not apply. Intraplate earthquakes tend to gather at the location of weak lithosphere (low-velocity zone) surrounding the strong lithosphere (very high-velocity zone) where the rheological contrast may cause stress accumulation and further trigger large earthquakes. This theory seems to be true considering the intraplate

earthquake distribution in our study area. Besides the factor of the lithospheric velocity contrast, the extrusion tectonics may also contribute to the occurrence of dense intraplate seismicity.

4.6 Conclusions

We have used Rayleigh wave tomography with a two-plane wave approach and a sensitivity kernel inversion to image the velocity and anisotropy structures beneath the northeastern Tibetan Plateau. Our phase velocity and shear wave velocity models both indicate that the lithosphere (0-100 km) in our study area can be divided into the low-velocity northeastern Tibetan Plateau and the high-velocity Ordos and Sichuan blocks with a sharp boundary at $\sim 105^\circ$ longitude. On the other hand, in the asthenosphere (125-200 km), we observe a low-velocity channel along the Qilian-Qinling Orogen that passes through the gap between the Ordos Plateau and the Sichuan Basin. We interpret it to be associated with the asthenospheric flow caused by the extrusion of the Tibet continent as a result of the Indo-Eurasia collision. Our anisotropy model in the whole study area shows a uniform NNW-SSE fast direction for all the periods (20-143 s) with large anisotropy amount at long periods (100-143 s). Our fast direction generally matches both SKS splitting data and the predicted strain field from GPS measurements. It suggests that the deformation occurs coherently from the crust to the asthenosphere in our study area with large deformation in the asthenosphere that may be related to the escape tectonics. Last, most large intraplate earthquakes in our study area appear to follow the boundary between the thin and thick lithospheric blocks at $\sim 105^\circ$ longitude. The

rheological difference together with the extrusion may trigger intense seismicity on the northeastern margin of the Tibetan Plateau.

4.7 Acknowledgements

We would like to thank helpful comments from Mian Liu with the interpretation of our tomographic models. We would also like to thank IRIS and PASSCAL for their support of the deployment of the INDEPTH-IV/ASCENT array. This work is supported by the Continental Dynamics program at the National Science Foundation, grant No. EAR0409589.

4.8 References

- An, M.J., and Y.L. Shi (2006), Lithospheric thickness of the Chinese continent, *Phys. Earth Planet. In.*, 159, 257-266, DOI: 10.1016/j.pepi.2006.08.002.
- Brown, L.D., W.J. Zhao, K.D. Nelson, M. Hauck, D. Alsdorf, A. Ross, M. Cogan, M. Clark, X.W. Liu, and J.K. Che (1996). Bright spots, structure, and magmatism in Southern Tibet from INDEPTH seismic reflection profiling, *Science*, 274, 1688-1691.
- Burchfiel, B.C., Z.L. Chen, Y.P. Liu, and L.H. Royden (1995), Tectonics of the Longmen Shan and adjacent regions, Central China, *International Geology Review*, 37, 661-735.
- Chang, L.J., C.Y. Wang, and Z.F. Ding (2008), Seismic anisotropy of upper mantle in Sichuan and adjacent regions, *Science in China Series D: Earth Sciences*, 51, 1683-1693.
- Clark, M.K., J. Bush, and L. Royden (2005), Dynamic topography produced by lower crustal flow against rheological strength heterogeneities bordering the Tibetan Plateau, *Geophys. J. Int.*, 162, 575-590.
- Clark, M.K., and L.H. Royden (2000), Topographic ooze: building the eastern margin of

- Tibet by lower crustal flow, *Geology*, 28, 703-706.
- Clifford, A.A. (1975), *Multivariate Error Analysis*, John Wiley, Hoboken, N. J.
- Duan, Y.H, X.K. Zhang, Z. Liu, Z.F. Xu, F.Y. Wang, J.S. Pan, and G.J. Liang (2007), Crustal structure using receiver function in the east part of Anyemaqen suture belt? *Acta Seismologica Sinica*, 20, 513-522.
- Enkelmann, E., L. Ratschbacher, R. Jonckheere, R. Nestler, M. Fleischer, R. Gloaguen, B.R. Hacker, Y.Q. Zhang, and Y.S. Ma (2006), Cenozoic exhumation and deformation of northeastern Tibet and the Qinling: Is Tibetan lower crustal flow diverging around the Sichuan Basin? *Geol. Soc. Am.*, 118, 651-671, doi: 10.1130/B25805.1.
- Flesch, L.M., W.E. Holt, P.G. Silver, M. Stephenson, C.Y. Wang, and W.W. Chan (2005), Constraining the extent of crust-mantle coupling in central Asia using GPS, geologic, and shear wave splitting data, *Earth Planet. Sci. Lett.*, 238, 248-268, DOI: 10.1016/j.epsl.2005.06.023.
- Flower, M., K. Tamaki, and N. Hoang (1998), Mantle extrusion: A model for dispersed volcanism and DUPAL-like asthenosphere in East Asia and the western Pacific. In: *Flower, M.F.J., Chung, S.-L., Lo, C.-H., Lee, T.-Y. (Eds.), Mantle Dynamics and Plate Interactions in East Asia, Geodynamics Series, American Geophysical Union, Washington, DC, pp. 67-88.*
- Forsyth, D.W., and A. Li (2005), Array analysis of two-dimensional variations in surface wave phase velocity and azimuthal anisotropy in the presence of multipathing interference, in *SeismicEarth: Array Analysis of Broadband Seismograms, Geophys. Monogr. Ser.*, vol. 157, edited by A. Levander and G. Nolet, pp. 81-97, AGU, Washington, D. C.
- Forsyth, D.W., S. Webb, L. Dorman, and Y. Shen (1998), Phase velocities of Rayleigh waves in the MELT experiment on the East Pacific Rise, *Science*, 280, 1235-1238.
- Friederich, W., and E. Wielandt (1995), Interpretation of seismic surface waves in regional networks: Joint estimation of wavefield geometry and local phase velocity. Method and tests, *Geophys. J. Int.*, 120, 731-744.
- Huang, J., and D. Zhao (2006), High-resolution mantle tomography of China and surrounding regions, *J. Geophys. Res.*, 111, B09305, doi:10.1029/2005JB004066.
- Huang, Z., M. Xu, L. Wang, N. Mi, D. Yu, and H. Li (2008), Shear wave splitting in the southern margin of the Ordos Block, north China, *Geophys. Res. Lett.*, 35, L19301, doi:10.1029/2008GL035188.
- Kennett, B.L.N., E.R. Engdahl, and R. Buland (1995), Constraints on seismic velocities

in the Earth from travel times, *Geophys. J. Int.*, 122, 108-124.

- Lev, E., M.D. Long, and R.D. van der Hilst (2006), Seismic anisotropy in Eastern Tibet from shear wave splitting reveals changes in lithospheric deformation, *Earth Planet. Sci. Lett.*, 251, 293-304.
- Li, A., and K. Burke (2006), Upper mantle structure of southern Africa from Rayleigh wave tomography, *J. Geophys. Res.*, 111, B10303, doi:10.1029/2006JB004321.
- Li, A., D.W. Forsyth, and K.M. Fischer (2003), Shear velocity structure and azimuthal anisotropy beneath eastern North America from Rayleigh wave inversion, *J. Geophys. Res.*, 108(B8), 2362, doi:10.1029/2002JB002259.
- Li, C., R.D. van der Hilst, A.S. Meltzer, and E.R. Engdahl (2008), Subduction of the Indian lithosphere beneath the Tibetan Plateau and Burma, *Earth Planet. Sci. Lett.*, 277, 157-168.
- Li H.Y., W. Su, C.Y. Wang, and Z.X. Huang (2009), Ambient noise Rayleigh wave tomography in western Sichuan and eastern Tibet, *Earth Planet. Sci. Lett.*, 282, 201-211, DOI: 10.1016/j.epsl.2009.03.021.
- Li, S.L., W.D. Mooney, and J.C. Fan (2006a), Crustal structure of mainland China from deep seismic sounding data, *Tectonophysics*, 420, 239-252.
- Li, Y.H., Q.J. Wu, Z.H. An, X.B. Tian, R.S. Zeng, R.Q. Zhang, and H.G. Li (2006b), The Poisson ratio and crustal structure across the NE Tibetan Plateau determined from receiver functions, *Chinese J. Geophys.*, (in Chinese) 49, 1359-1368.
- Liang, C.T. and X.D. Song (2006), A low velocity belt beneath northern and eastern Tibetan Plateau from Pn tomography, *Geophys. Res. Lett.*, 33, L22306, doi:10.1029/2006GL027926.
- Liu, M., X.J. Cui, and F.T. Liu (2004), Cenozoic rifting and volcanism in eastern China: a mantle dynamic link to the Indo-Asian collision? *Tectonophysics*, 393, 29-42.
- Lou, H., C.Y. Wang, Z.Y. Lu, Z.X. Yao, S.G. Dai, and H.C. You (2009), Deep tectonic setting of the 2008 Wenchuan Ms8.0 earthquake in southwestern China - Joint analysis of teleseismic P-wave receiver functions and Bouguer gravity anomalies, *Science in China Series D: Earth Sciences*, 52, 166-179.
- Molnar, P., and P. Tapponnier (1975), Cenozoic tectonics of Asia: effects of a continental collision, *Science*, 189, 419-426.
- Pei, S.P., J.M. Zhao., Y.S. Sun, Z.H. Xu, S.Y. Wang, H.B. Liu., C.A. Rowe, M.N. Toksoz, and X. Gao (2007), Upper mantle seismic velocities and anisotropy in China determined through Pn and Sn tomography, *J. Geophys. Res.*, 112, B05312,

doi:10.1029/2006JB004409.

- Royden, L.H., B.C. Burchfiel, R.W. King, E. Wang, Z.L. Chen, F. Shen, and Y.P. Liu (1997), Surface deformation and lower crustal flow in eastern Tibet, *Science*, 276, 788-790.
- Royden, L.H., B. C. Burchfiel, and R.D. van der Hilst (2008), The Geological Evolution of the Tibetan Plateau, *Science*, 321, 1054-1058.
- Saito, M. (1988), DISPER80: A subroutine package for the calculation of seismic normal-mode solutions, in *Seismological Algorithms*, edited by D. J. Doornbos. Elsevier, New York, 293-319.
- Smith, M.L., and F.A. Dahlen (1973), The azimuthal dependence of Love and Rayleigh wave propagation in a slightly anisotropic medium, *J. Geophys. Res.*, 78, 3321-3333.
- Su, W., C.Y. Wang, and Z.X. Huang (2008), Azimuthal anisotropy of Rayleigh waves beneath the Tibetan Plateau and adjacent areas, *Science in China Series D: Earth Sciences*, 51, 1717-1725.
- Sun, Y.S., M.N. Toksoz, S.P. Pei, D.P. Zhao, F.D. Morgan, and A. Rosca (2008), S wave tomography of the crust and uppermost mantle in China, *J. Geophys. Res.*, 113, B11307, doi:10.1029/2008JB005836.
- Tapponnier, P., and P. Molnar (1977), Active faulting and tectonics in China, *J. Geophys. Res.*, 82, 2905-2930.
- Tapponnier, P., Z. Xu, F. Roger, B. Meyer, N. Arnaud, G. Wittlinger, and J. Yang (2001), Oblique stepwise rise and growth of the Tibet Plateau, *Science*, 294, 1671-1677.
- Tarantola, A., and B. Valette (1982), Generalized non-linear problems solved using the least-squares criterion, *Rev. Geophys.*, 20, 219-232.
- Tilmann, F., J. Ni, and INDEPTH III Team (2003), Seismic imaging of the downwelling Indian lithosphere beneath central Tibet, *Science*, 300, 1424-1427, doi: 10.1126/science.1082777.
- Tong, W.W., L.S. Wang, N. Mi, M.J. Xu, H. Li, D.Y. Yu, C. Li, S.W. Liu, M. Liu, and E. Sandvol (2007), Receiver function analysis for seismic structure of the crust and uppermost mantle in the Liupanshan area, China, *Science in China Series D: Earth Sciences*, 50, 227-233.
- Wang, C.Y., L.M. Flesch, P.G. Silver, L.J. Chang, and W.W. Chan (2008), Evidence for mechanically coupled lithosphere in central Asia and resulting implications, *Geology*, 36, 363-366, DOI: 10.1130/G24450A.1.

- Yang, Y.J., and D.W. Forsyth (2006a), Regional tomographic inversion of the amplitude and phase of Rayleigh waves with 2-D sensitivity kernels, *Geophys. J. Int.*, 166, 1148-1160.
- Yang, Y.J., and D.W. Forsyth (2006b), Rayleigh wave phase velocities, small-scale convection, and azimuthal anisotropy beneath southern California, *J. Geophys. Res.*, 111, B07306, doi:10.1029/2005JB004180.
- Yin, A., and T.M. Harrison (2000), Geologic evolution of the Himalayan-Tibetan orogen, *Annu. Rev. Earth Planet. Sci.*, 28, 211-280.
- Zhang, Q., E. Sandvol, and M. Liu (2009a), Tomographic Pn velocity and anisotropy structure in the central and eastern United States, *Bull. Seismol. Soc. Am.*, 99, 422-427.
- Zhang, Q., E. Sandvol, and M. Liu (2009b), Lithospheric velocity structure of the New Madrid Seismic Zone: A joint teleseismic and local P tomographic study, *Geophys. Res. Lett.*, 36, L11305, doi:10.1029/2009GL037687.
- Zhang, Y.Q., J.L. Mercier, and P. Vergely (1998), Extension in the graben systems around the Ordos (China), and its contribution to the extrusion tectonics of south China with respect to Gobi-Mongolia, *Tectonophysics*, 285, 41-75, DOI: 10.1016/S0040-1951(97)00170-4.
- Zhao W., K.D. Nelson, and Project INDEPTH (1993), Deep seismic reflection evidence for continental underthrusting beneath southern Tibet, *Nature*, 366, 557-559.
- Zhou, Y., F.A. Dahlen, and G. Nolet (2004), Three-dimensional sensitivity kernels for surface wave observables, *Geophys. J. Int.*, 158, 142-168.

CHAPTER 5: CONCLUSIONS

5.1 Conclusions

To investigate the nature and cause of the intraplate earthquakes, I used seismic tomography approaches to establish the velocity and anisotropy models of some of the most significant intraplate seismic zones in the world. My first study on Pn tomography in the Central and Eastern United States (CEUS) reveals a strong correlation between the edges of the high-velocity anomalies in the lithospheric mantle with the locations of major intraplate seismic zones (the New Madrid seismic zone, the East Tennessee seismic zone, the Charleston seismic zone, and the New England seismic zone). This correlation may be explained by the stress concentration near the rheological boundaries in the lithosphere. My Pn anisotropy results also indicate focused mantle flow around the edges of the high-velocity blocks. Such mantle shearing zones may further contribute to the stress localization and intraplate seismicity in the CEUS. On the other hand, my Pn tomographic model does not support the perception that the ancient rifts in the CEUS are linked to low-velocity anomalies (presumably weak zones) in the lithospheric mantle. Based on the lack of spatial association between the ancient rifts and the major intraplate seismic zones in the CEUS, I suggest that the ancient rifts are not the primary factor causing the large seismic events in the CEUS.

My second study has modeled the lithospheric velocity structure of the New Madrid seismic zone (NMSZ) using a combination of teleseismic P and local P travel-time data. The tomographic results show that the NMSZ seismicity and faults are

underlain by a localized low-velocity anomaly in the lower crust and upper mantle which is primarily confined within and parallel to the Reelfoot rift. On the other hand, my results do not show a compelling evidence for dense mafic intrusions in the lower crust that have been proposed. The low-velocity anomaly under the NMSZ may represent a deep shear zone at rheological boundaries, considering the results from the previous Pn tomography. Such a weak zone could shift stress to the upper crust, and thus helps explain the repeated shallow earthquakes in the NMSZ where the present-day strain rate is near zero.

My third study has used Rayleigh wave tomography to image the velocity and anisotropy structures beneath the northeastern Tibetan Plateau where intense intraplate seismicity occurred. My velocity models indicate that the lithosphere (0-100 km) can be divided into the low-velocity northeastern Tibetan Plateau and the high-velocity Ordos and Sichuan blocks with a sharp boundary at $\sim 105^\circ$ longitude. In the asthenosphere (125-200 km), I observe a low-velocity channel along the Qilian-Qinling Orogen that passes through the gap between the Ordos Plateau and the Sichuan Basin. It is probably associated with the asthenospheric flow caused by the extrusion. My anisotropy model in the whole study area shows a uniform NNW-SSE fast direction for all the periods (20-143 s) with large anisotropy amount at long periods (100-143 s). The fast direction generally matches both SKS splitting data and the predicted strain field from GPS measurements. It suggests that the deformation occurs coherently from the crust to the asthenosphere in the study area with large deformation in the asthenosphere that may be related to the escape tectonics. Last, most large intraplate earthquakes in the study area appear to follow the boundary between the thin and thick lithospheric blocks at $\sim 105^\circ$

longitude. The rheological difference together with the extrusion may trigger intense seismicity on the northeastern margin of the Tibetan Plateau.

All of the above three studies point to the idea that the lithospheric velocity contrast plays an important role for the occurrence of intraplate earthquakes. The high and low velocity boundary may present a rheological transition zone that separates the strong and weak lithosphere. Kuszniir and Park's (1982, 1984) mathematical modeling has shown that a structure of ductile/weak lower lithosphere and brittle/strong upper lithosphere can cause stress decay and amplification in the lower and upper lithosphere, respectively. Such a stress shift process could contribute to the stress accumulation at the edge of the brittle lithosphere, and further cause complete fractures or a whole lithosphere failure. This idea matches my velocity model in the NMSZ where the velocity contrast (presumably rheological contrast) probably transfers the stress upwards to the relatively high-velocity upper crust and triggers significant intraplate earthquakes. This stress amplification theory applies to the lateral velocity boundaries too, where the intraplate earthquakes are concentrated. Li et al.'s (2007) numerical calculation has predicted large Coulomb stress focused in the areas of relatively thin lithosphere, around the margin of thick lithospheric roots. The stress accumulation process is a function of the geothermal structure in the lithosphere. For very weak or "hot" lithosphere, only small applied stress and time are required to cause geologically significant deformation. An alternative thought is that the mantle flow around thick lithospheric roots may cause deformation at the edges of the rigid lithosphere. For example, Fouch et al.'s (2000) SKS splitting data indicate that significant anisotropy occurs around the lithospheric root beneath the North American craton. This sub-lithospheric flow occurs deeply and its influence on the crust

may not be as significant as the previous mechanism.

5.2 References

- Fouch, M.J., K.M. Fischer, E.M. Parmentier, M.E. Wysession, and T.J. Clarke (2000), Shear wave splitting, continental keels, and patterns of mantle flow, *J. Geophys. Res.*, 105, 6255-6275.
- Kusznir, N.J., and R.G. Park (1982), Intraplate lithosphere strength and heat flow, *Nature*, 299, 540-542.
- Kusznir, N.J., and R.G. Park (1984), Intraplate lithosphere deformation and the strength of the lithosphere, *Geophys. J. Roy. Astron. Soc.*, 79, 513-538.
- Li, Q., M. Liu, Q. Zhang, and E. Sandvol (2007), Stress evolution and seismicity in the central-eastern United States: insights from geodynamic modeling, in Continental Intraplate Earthquakes: Science, Hazard, and Policy Issues, *Geol. Soc. Am. Special Paper*, 425, 149–166.

VITA

Qie Zhang was born in Hubei Province, China. He received his B.S. in Geology from Nanjing University, China in 2002 and M.S. in Structural Geology from Nanjing University, China in 2004. He began his doctoral study in United States in 2004 and received Ph.D. in Geophysics (Seismology) in 2009. He will join the advanced seismic imaging team of BP at Houston, Texas in October, 2009.